3-24-2016

Forecasting Sea Breeze Enhanced Thunderstorms at Eglin Air Force Base: A Comparison Between Empirical Methods and the High Resolution Rapid Refresh Model

Matthew P. King

Recommended Citation

King, Matthew P., "Forecasting Sea Breeze Enhanced Thunderstorms at Eglin Air Force Base: A Comparison Between Empirical Methods and the High Resolution Rapid Refresh Model" (2016). *Theses and Dissertations*. 342.
https://scholar.afit.edu/etd/342

FORECASTING SEA BREEZE ENHANCED THUNDERSTORMS AT EGLIN AIR FORCE BASE: A COMPARISON BETWEEN EMPIRICAL METHODS AND THE HIGH RESOLUTION RAPID REFRESH MODEL

THESIS

Matthew P. King, Capt, USAF

AFIT-ENP-MS-16-M-074

DEPARTMENT OF THE AIR FORCE
AIR UNIVERSITY

AIR FORCE INSTITUTE OF TECHNOLOGY

Wright-Patterson Air Force Base, Ohio

DISTRIBUTION STATEMENT A
APPROVED FOR PUBLIC RELEASE; DISTRIBUTION UNLIMITED.

AFIT-ENP-MS-16-M-074

FORECASTING SEA BREEZE ENHANCED THUNDERSTORMS AT EGLIN AIR FORCE BASE:
A COMPARISON BETWEEN EMPIRICAL METHODS AND THE HIGH RESOLUTION RAPID REFRESH MODEL

THESIS

Presented to the Faculty
Department of Engineering Physics
Graduate School of Engineering and Management
Air Force Institute of Technology
Air University
Air Education and Training Command
in Partial Fulfillment of the Requirements for the
Degree of Master of Science in Applied Physics

Matthew P. King, B.S.
Capt, USAF

March 24, 2016

DISTRIBUTION STATEMENT A
APPROVED FOR PUBLIC RELEASE; DISTRIBUTION UNLIMITED.

AFIT-ENP-MS-16-M-074

FORECASTING SEA BREEZE ENHANCED THUNDERSTORMS AT EGLIN AIR FORCE BASE:

A COMPARISON BETWEEN EMPIRICAL METHODS AND THE HIGH RESOLUTION RAPID REFRESH MODEL

THESIS

Matthew P. King, B.S.
Capt, USAF

Committee Membership:

Lt Col Kevin S. Bartlett, PhD
Chair

Lt Col Robert S. Wacker, PhD
Member

Robert D. Loper, PhD
Member

Lt Col Robert A. Stenger, PhD
Member

AFIT-ENP-MS-16-M-074

Abstract

Summer thunderstorms pose the greatest forecast challenge for the United States Air Force's 96th Weather Flight (96 WF) which provides weather support for Eglin Air Force Base (AFB). Located on Florida's panhandle, Eglin AFB encompasses the Department of Defense's largest range complex which covers 134,000 mi^2 ($347,000\ km^2$) of water and 724 mi^2 ($1875\ km^2$) of land. Due to the base's coastal location and unique coastline geometry, sea breeze is a dominant forecast consideration for thunderstorms. The 96 WF currently utilizes an empirical method, called WINNDEX, developed by former staff meteorologist Roger Winn to aid in thunderstorm forecasts. It combines the use of 12 UTC sounding data and nomograms to provide a forecast for Eglin's main base area and its land range. This study sought to compare the forecasts of the High Resolution Rapid Refresh (HRRR) model and WINNDEX. Final results indicated HRRR forecast skill surpassed WINNDEX in most metrics which included percent correct, probability of detection, false alarm rate, bias, critical skill index, Heidke Skill Score, Peirce Skill Score, and timing error.

Acknowledgements

Completing this Master's degree at AFIT would have been impossible without the love and encouragement of my wife and daughters. I can not thank you all enough for your patience and understanding over the nearly two years we have spent here. The future will hold new adventures for us as we move on from here, but I will always cherish the memories and lessons we gained. Also, to my Mom, I am so appreciative for your help when we needed it during those rough times. I would like to thank my professors, particularly Lt Col Wacker, Lt Col Bartlett, and Dr. Loper for all their guidance through the classes, the thesis research, and the whole AFIT experience. Additionally, I would like to thank Mr. Biggar for his role as my point of contact for my thesis topic as well as the one on one time with Mr. Curry who was kind of enough to share his expertise of WINNDEX. I'd also like to thank the men and women of the 96th Weather Flight for letting me see what you all do everyday. Additionally, I would like to thank Mr. Zautner and the team at the 14th Weather Squadron who ensured I had all the required lightning data for this thesis. Lastly, I want to thank all my classmates, MacLane, Fred, Derek, and Kyle, for helping me when I needed it during those difficult times. I'll definitely miss all the "fun" times we had at AFIT and I look forward to seeing you all again.

Matthew P. King

Table of Contents

Page

List of Figures

Figure Page

Figure Page

FORECASTING SEA BREEZE ENHANCED THUNDERSTORMS AT EGLIN
AIR FORCE BASE:
A COMPARISON BETWEEN EMPIRICAL METHODS AND THE HIGH
RESOLUTION RAPID REFRESH MODEL

I. Introduction

1.1 Motivation

Eglin Air Force Base (AFB), which provides support for aircraft and munitions testing as well as developmental and operational testing and pilot training for the F-35 Joint Strike Fighter, encompasses the Department of Defense's (DoD) largest range which covers 134,000 mi^2 ($347,000\ km^2$) of water and 724 mi^2 ($1875\ km^2$) of land (Homan 2015). In the summer season, Eglin AFB is frequently affected by sea breeze thunderstorms which can cause limitations and delays to testing and operations. The 96th Weather Flight (96 WF), which provides weather support for the base and its units, considers sea breeze thunderstorms to be the most mission limiting weather phenomenon at Eglin AFB. Because of the difficulty of accurately forecasting sea breeze thunderstorms, forecasters and staff meteorologists since the 1960s have attempted to create better focused tools to forecast them. In the continuing endeavor to improve forecast accuracy, this study attempts to find additional forecast skill using high resolution numerical weather prediction.

1.2 Eglin Geography and Climatology

1.2.1 Geography.

Located in the western Florida panhandle between Pensacola and Panama City, FL as shown in Figure 1, Eglin AFB is in one of the most convectively active regions in the United States due to its proximity to the Gulf Coast (Weaver 2006).

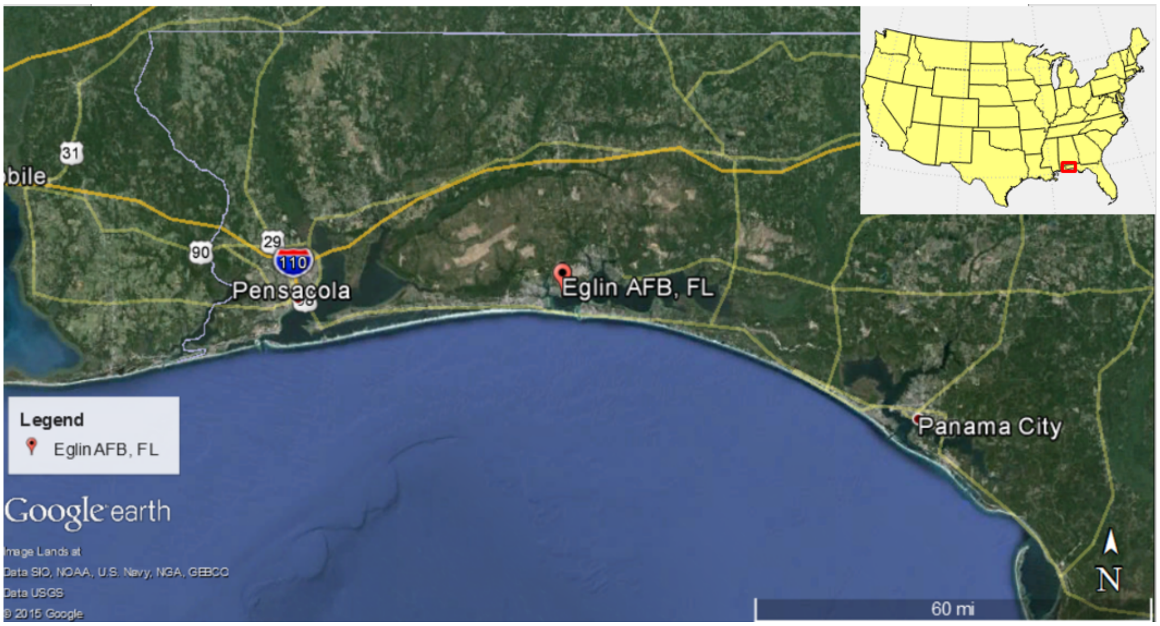

Figure 1. Eglin AFB location.

The forecast area in this study is the Eglin range complex which includes Eglin AFB and the Eglin reservation. The complex totals 724 mi^2 (1875 km^2) of varied multi-environmental land area with 45 test areas, 34 test systems/facilities, and 26 multipurpose systems/facilities for testing and evaluation of munitions and weapons systems (Weaver 2006). As indicated in Figure 2, the range complex measures 34 km from south to north and 81 km from east to west. The range complex reaches its highest point at 250 feet on the northwest corner and is bordered along the north by rivers and by creeks to the east (Weaver 2006). The terrain consists of both flat areas and gentle rolling hills that are covered with woods of pine trees and scrub oak

(Weaver 2006). In addition, the coastline geometry is complex with the East Bay to the southwest, the Gulf of Mexico to the south, and the Choctawhatchee Bay to the southeast of the range complex. This unique coastline adds complexity to the sea breeze circulation.

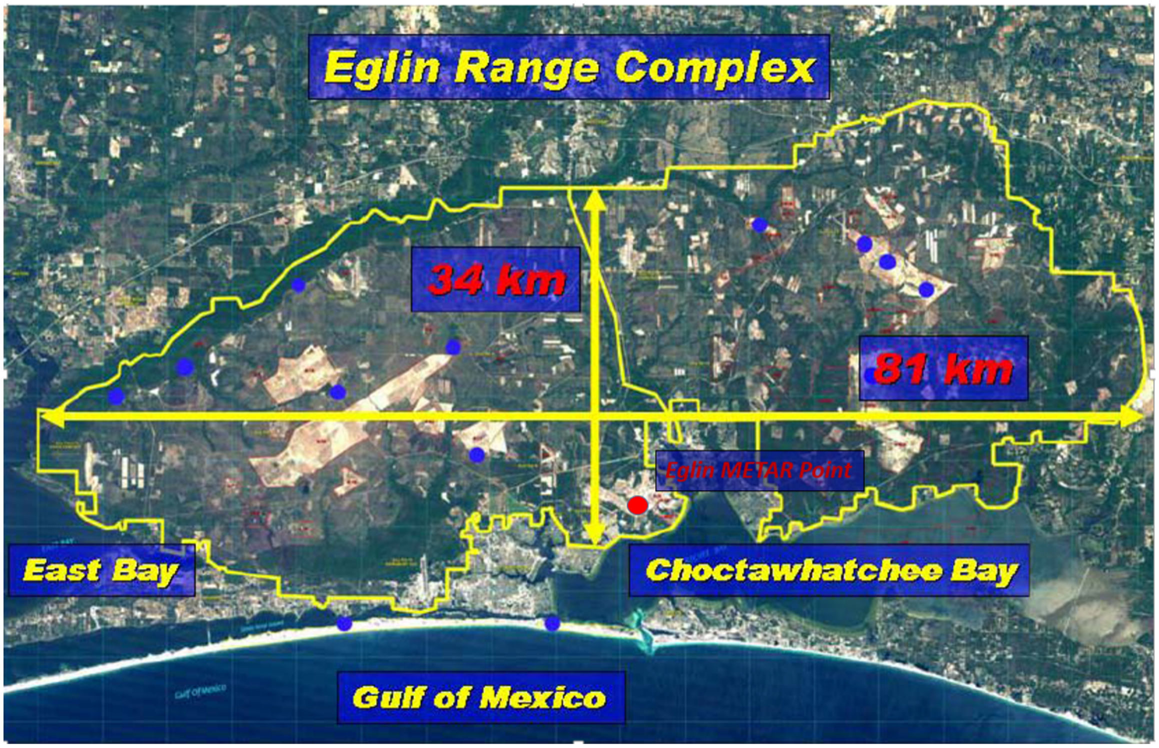

Figure 2. Eglin Range Complex. Adapted from Weaver (2006).

1.2.2 Climatology.

According to specifc climatology for Eglin AFB from the 14th Weather Squadron's Operational Climatic Data Summary (OCDS), based on a mean period of record from January 2000 to December 2014, there are on average 92 thunderstorm days per year, of which 70 occur between May and September (14th Weather Squadron 2015). The period between May and September — typically referred to as the "warm season" for Eglin AFB — is distinct due to considerably warm temperatures. It is because of the warm temperatures that the sea breeze becomes an important forecast consideration. Figure 3 provides climatological temperatures for Eglin AFB based on the OCDS.

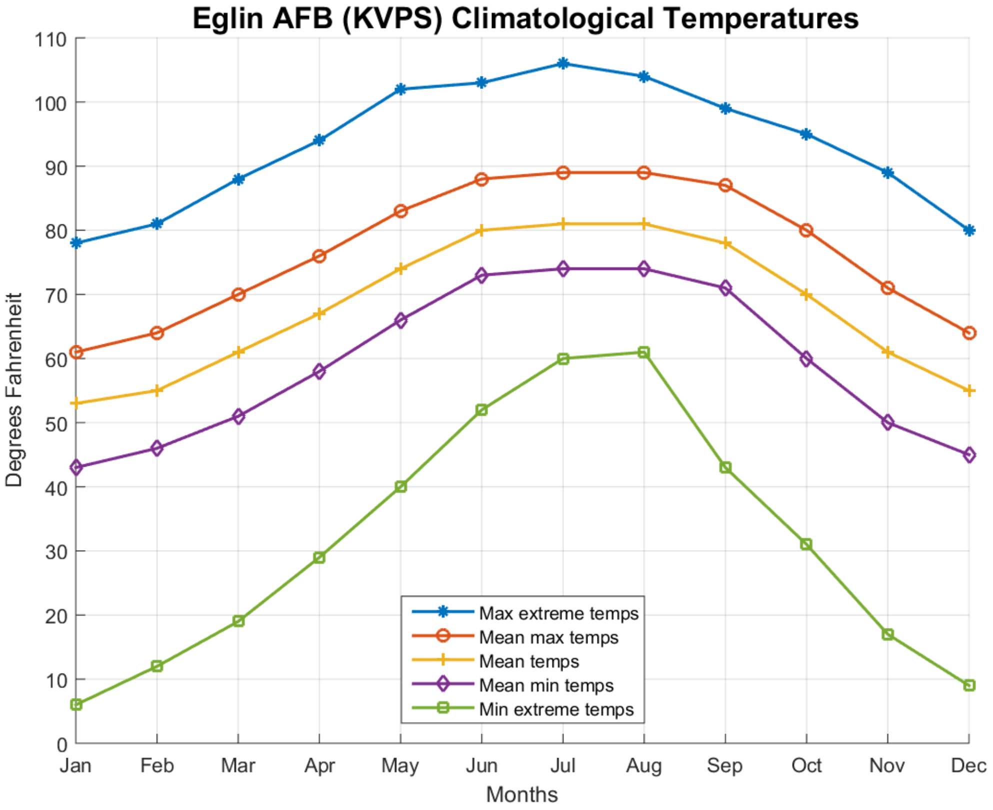

Figure 3. Climatological temperatures for Eglin AFB based on OCDS data from 14th Weather Squadron (2015).

In Figure 4 the annual lightning flash density over the continental United States (CONUS) indicates that the Florida Panhandle has a local maximum in thunderstorm activity. The warm season maximum in thunderstorm occurrence is attributed primarily to the daily sea breeze cycle and the associated sea breeze front (Weaver, 2006). Although thunderstorm formation along the sea breeze front is a nearly daily occurrence in the summer, the time of initial onset and location of thunderstorms can vary significantly. This is due to daily variability of low-level synoptic-scale flow and the subsequent changes in low-level convergence and inland extent of the sea breeze front (Weaver 2006).

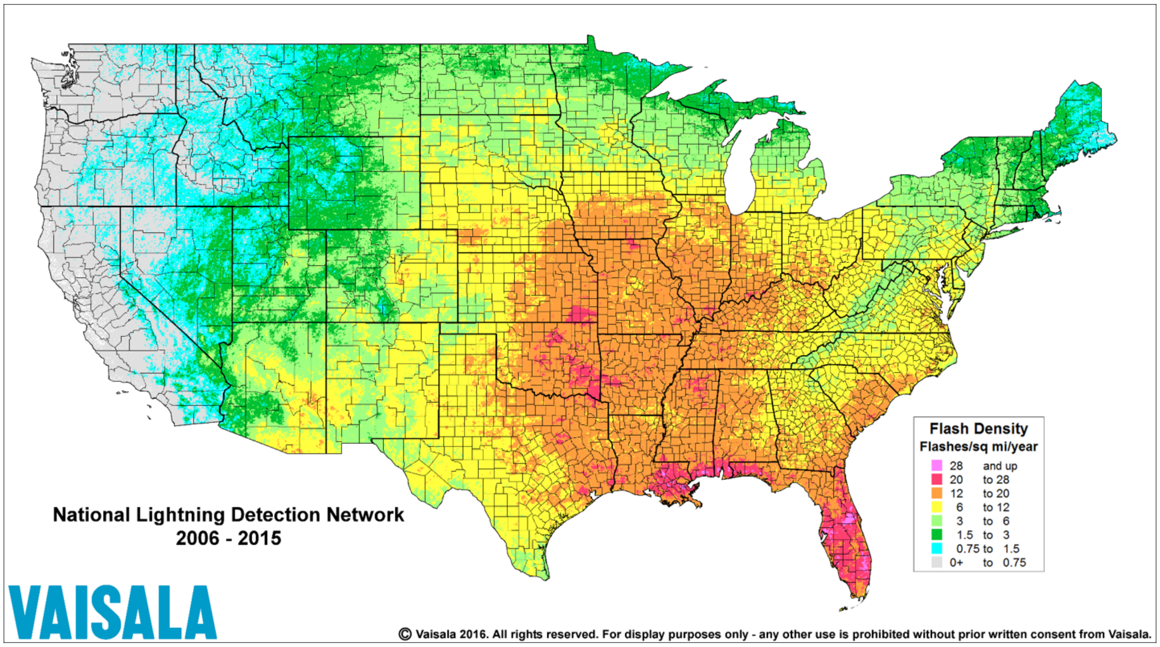

Figure 4. Vaisala National Lightning Detection Network CONUS flash density map. Annual flash density data encompasses the years 2005 through 2015 (Vaisala 2015).

Also provided by the OCDS is thunderstorm frequency based on time of day. The OCDS thunderstorm frequency data is organized in three hour periods. Figures 5 - 9 provide thunderstorm frequency data for months May - September while Figure 10 provides the frequency for the entire warm season. It is evident that thunderstorm frequency increases through months May and June and peaks in July. All months with the exception of September have peak thunderstorm frequency between 17 and 19 UTC. September thunderstorm frequency peaks between 20 and 22 UTC. However, for the entire warm season thunderstorm frequency peaks between 17 and 19 UTC with frequency between 20 and 22 UTC only about 1 percent lower. These thunderstorm frequencies show that the majority of thunderstorm activity over Eglin AFB is strongly related to warm temperatures and the diurnal heating cycle.

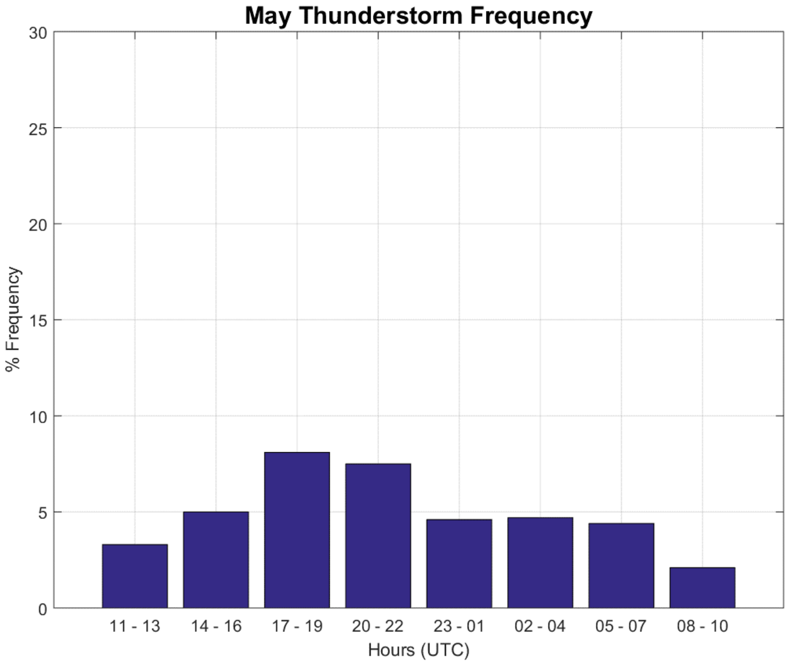

Figure 5. Eglin AFB thunderstorm frequency based on time of day for the month of May. Data from OCDS (14th Weather Squadron 2015).

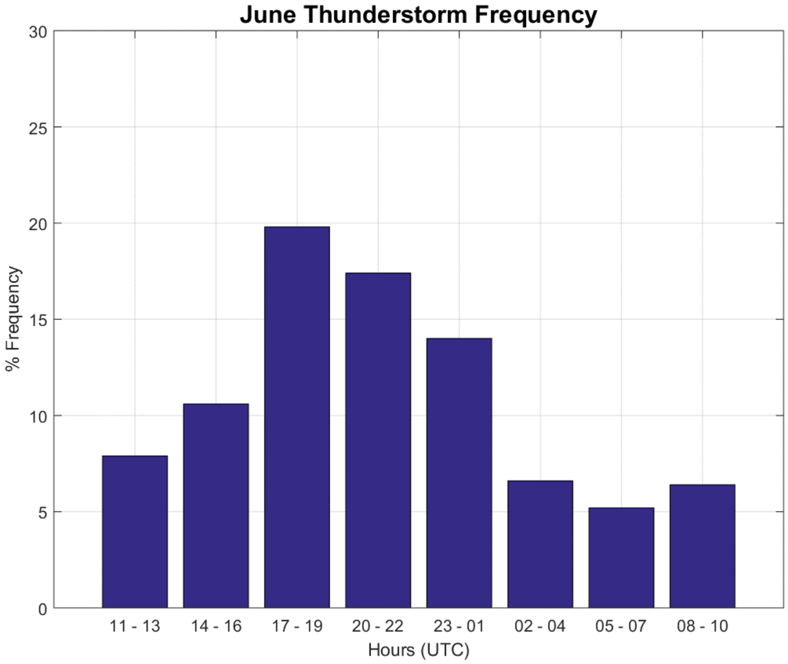

Figure 6. Eglin AFB thunderstorm frequency based on time of day for the month of June. Data from OCDS (14th Weather Squadron 2015).

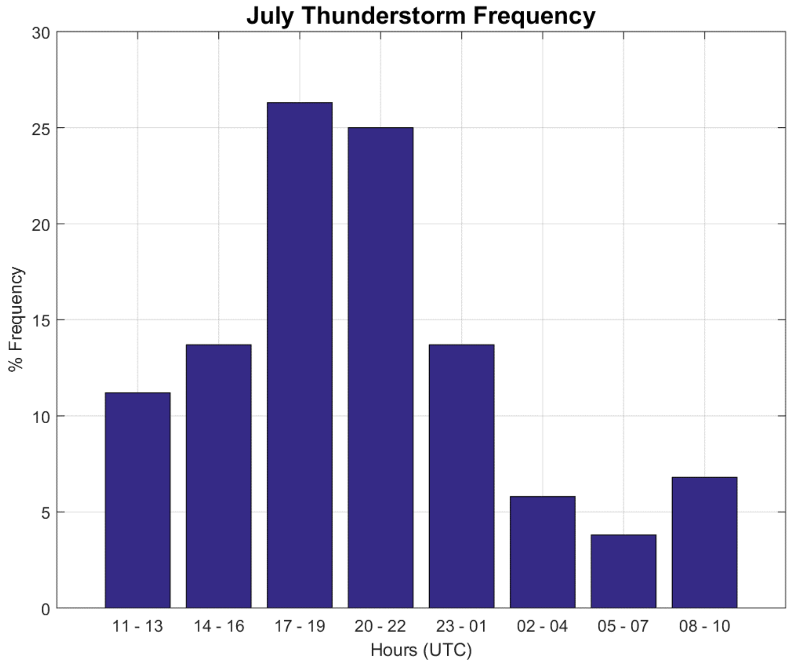

Figure 7. Eglin AFB thunderstorm frequency based on time of day for the month of July. Data from OCDS (14th Weather Squadron 2015).

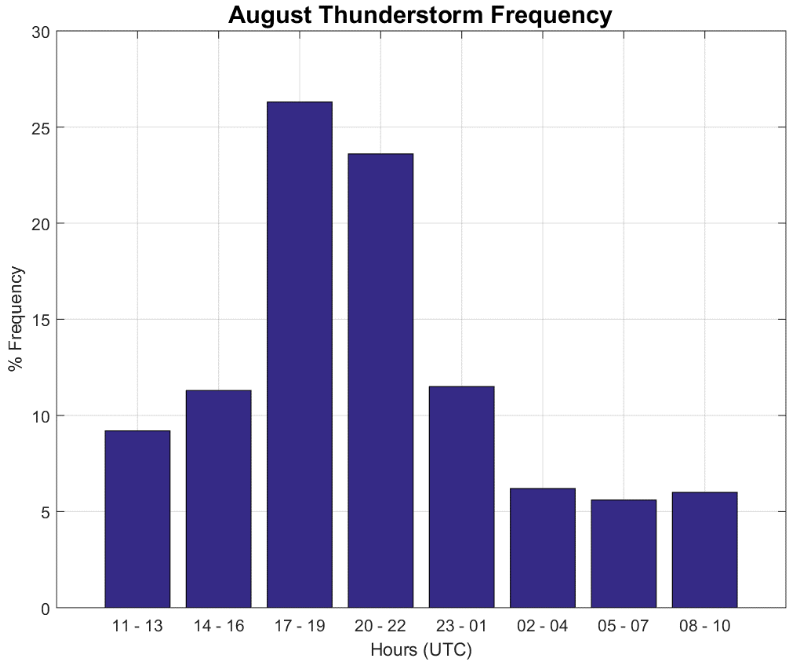

Figure 8. Eglin AFB thunderstorm frequency based on time of day for the month of August. Data from OCDS (14th Weather Squadron 2015).

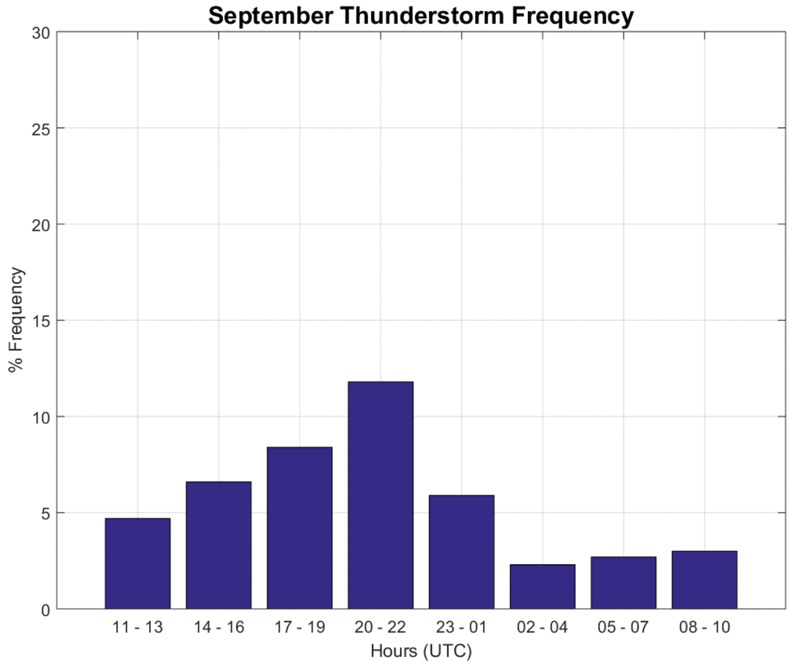

Figure 9. Eglin AFB thunderstorm frequency based on time of day for the month of September. Data from OCDS (14th Weather Squadron 2015).

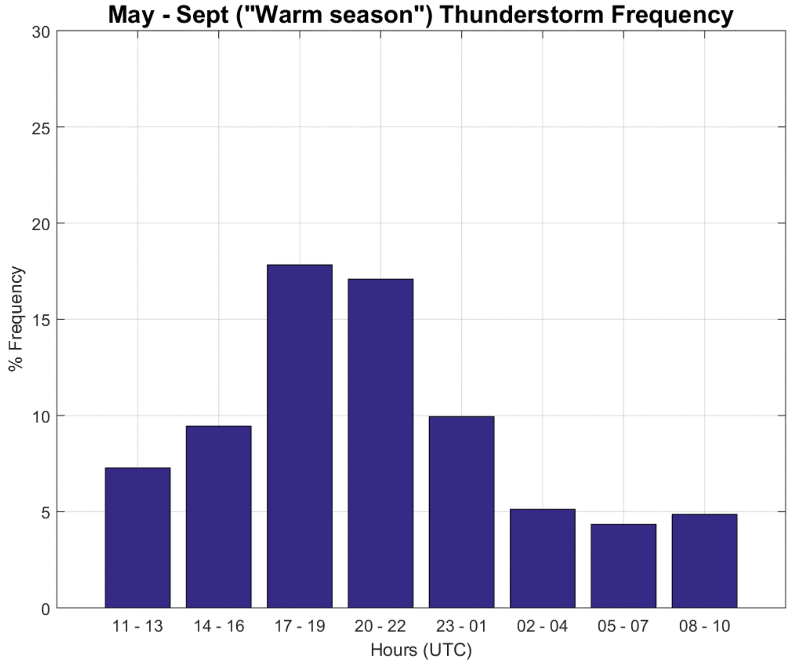

Figure 10. Eglin AFB thunderstorm frequency based on time of day for the months May through September. Data derived from OCDS (14th Weather Squadron 2015).

1.3 Current Forecast Method: WINNDEX

To date the best sea breeze thunderstorm forecasting method for Eglin AFB is WINNDEX, an empirical tool developed by former Eglin AFB staff meteorologist Roger Winn, who used data from June to September of 1986. WINNDEX was originally designed to utilize Eglin AFB radiosonde data, specifically 2000 ft (600 m) wind direction and speed, dew point depression at 700, 600, and 500 mb, convective condensation level (CCL), and wind direction at 12,000 (3700 m), 14,000 (4300 m), and 16,000 ft (4900 m). However, today Eglin AFB no longer launches radiosondes on a regular basis, but instead launches only when operations and testing require the upper-air data. Consequently, the 96 WF utilizes vertical profiles derived from numerical weather prediction data as well as observed soundings from nearby Tallahassee, FL and Slidell, LA to obtain the values needed to utilize WINNDEX.

1.3.1 WINNDEX Process.

To utilize WINNDEX, forecasters follow several steps:

(a) Using available skew-t data, compute the CCL.

(b) Compute sum of the dew point depressions at 700, 600, and 500 mb pressure levels.

(c) Determine primary wind component at upper-levels between 12,000 - 16,000 ft (3700 - 4900 m).

(d) Determine primary wind component at 2000 ft (600 m).

(e) Select appropriate nomogram from Figure 11 based on the average primary component of the 12,000 to 16,000 ft (3700 $-$ 4900 m) wind, and the 2000 ft (600 m) wind (ie. Northerly or Southerly).

(f) Utilizing the selected nomogram, match CCL and dew point depression sum to determine likely time frame and location of thunderstorms or showers.

Once the dew point depression sum and CCL are obtained and matched to the appropriate nomogram, WINNDEX indicates a time frame during which thunderstorms or rain showers are expected. This forecast provides a time frame for the main Eglin base area and a separate time frame for Eglin's range complex.

1.3.2 WINNDEX Limitations.

It was indicated in previous research by Weaver (2006) that WINNDEX, despite its usefulness, is too general in its forecast of thunderstorm development as it provides a blanket forecast for the entire Eglin range complex. For example, if thunderstorms formed only along the coastline, this situation would allow other portions of the range to be utilized; however, WINNDEX can not indicate a section of the range complex to aid in operational planning (Weaver 2006).

The second limitation to WINNDEX is in its nomogram design. There are four nomograms which are selected based on the north or south direction of low-level winds (2000 ft) and upper-level winds (12,000 - 16,000 ft). Because there is no information about eastward or westward components, the WINNDEX forecasts may be too generalized.

Lastly, WINNDEX was developed using data from only one warm season, specifically May - September of 1986 (Cornell 1993). Because WINNDEX is only based on one warm season, the data its forecasts are derived may be insufficient to provide a fully comprehensive forecast tool.

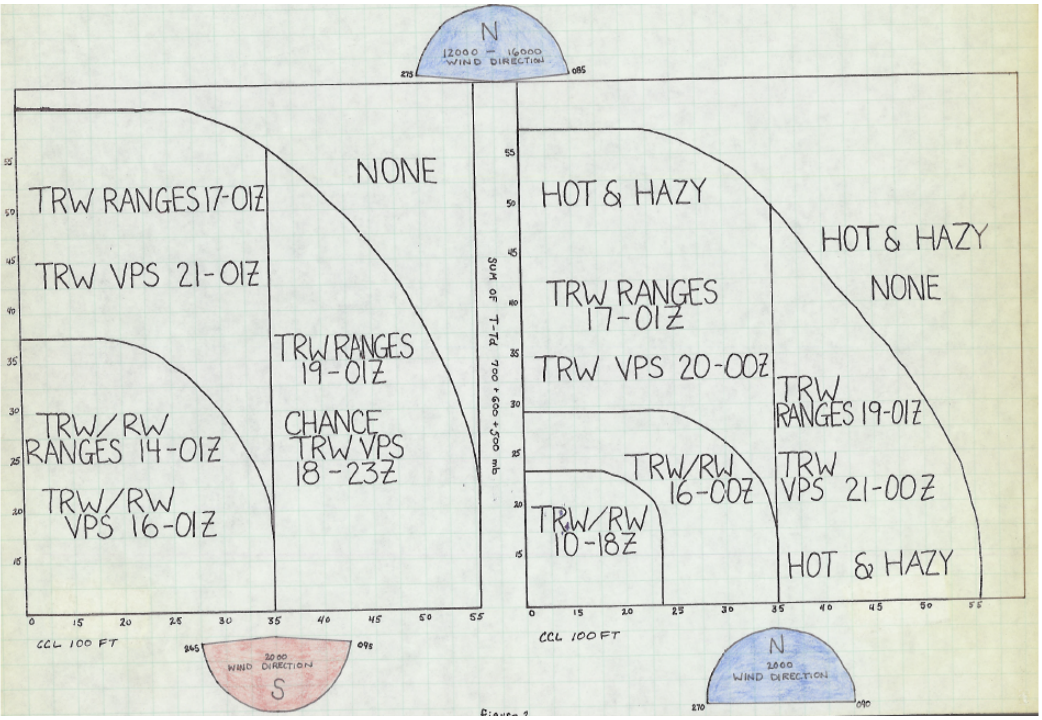

(a) Nomograms for northerly upper-level winds

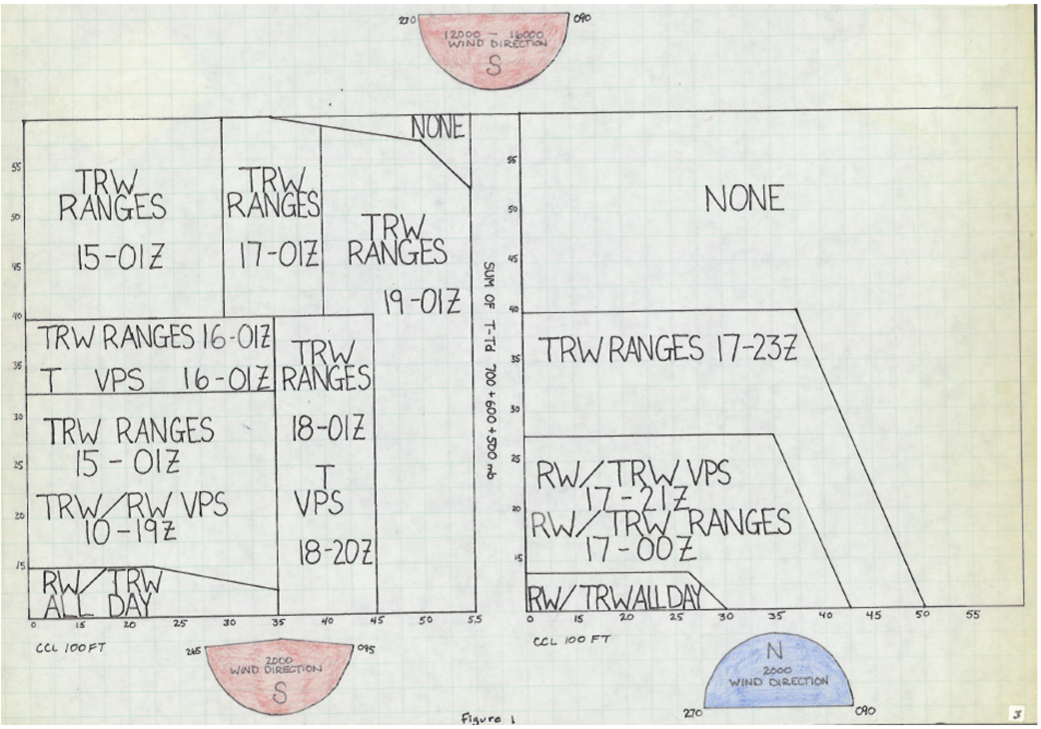

(b) Nomograms for southerly upper-level winds

Figure 11. WINNDEX nomograms utilizing CCL height and the sum of the dew point depression at 500, 600, and 700 mb pressure levels (Winn 1995).

1.4 Research Objective

With the progress of high resolution numerical weather prediction, there is a possibility that models have reached the level of detail and accuracy required to outperform empirical methods that have been tested and relied upon for many years in operations. The High Resolution Rapid Refresh (HRRR) is a high resolution model that has shown potential in forecasting sea breeze thunderstorms at Eglin AFB based on personal accounts from forecasters. Thus, it is the objective of this study to compare the forecast skill of WINNDEX and the HRRR to determine if high resolution numerical weather prediction has the ability to outperform an empirical sea breeze thunderstorm forecast method.

1.5 Preview

This chapter has briefly introduced the current state of forecasting sea breeze thunderstorms at Eglin AFB as well as the general scope of the objective of improving forecast skill. Chapter II provides in-depth background into the characteristics of sea breeze circulation and the associated thunderstorms that it helps to develop as well as previous research of WINNDEX performance, sea breeze circulation, and modeling associated with sea breeze thunderstorms. Chapter III summarizes the methodology of comparing WINNDEX performance with HRRR model output. Chapter IV explains research results and data analysis. Finally, Chapter V provides conclusions and recommendations for future work.

II. Background

2.1 Airmass Thunderstorms

Wallace and Hobbs (2006) define ordinary thunderstorms, or airmass thunderstorms, as "small isolated cumulonimbus clouds produced by local convection in an unstable airmass rather than by fronts or instability lines." They explain further that as single cell storms, air mass thunderstorms are typically short lived due to their development under weak vertical wind shear conditions. With weak wind shear conditions, the updraft within the storm is destroyed by the downdraft and the precipitation that the updraft helped to create (Wallace and Hobbs 2006).

2.1.1 Airmass Thunderstorm Life Cycle.

In the late 1940s, a field program known as the Thunderstorm Project researched a large number of airmass thunderstorms over Florida and Ohio to create an idealized model of the life cycle of a typical single-cell thunderstorm (Wallace and Hobbs 2006). Byers and Braham Jr. (1948), using findings from the Thunderstorm Project, found that single-cell thunderstorms undergo three distinct stages: cumulus, mature, and dissipating stages. The cumulus stage, consists of entirely warm, buoyant air with updraft velocities that increase rapidly with height within the cloud while gentle subsidence occurs in the surrounding environment (Byers and Braham Jr. 1948). With the strengthening updraft of warm, moist air, water is continually condensed to the eventual point that the resulting water droplets exceed the updraft's ability to keep the droplets aloft, thus precipitation is initiated and a resulting downdraft circulation begins, thereby marking the start of the mature stage (Byers and Braham Jr. 1948). As precipitation develops throughout the cloud, the downdraft circulation gradually becomes more extensive and eventually reaches the time at which it encompasses more of the cloud than the updraft in the dissipating stage (Byers and Braham Jr. 1948). With continual entrainment of outside environmental air into the cloud during the dissipating stage, the previously clear boundaries of the storm cell become indistinct and indicate the end of the storm's life cycle (Byers and Braham Jr. 1948). These three thunderstorm stages and their typical circulations are illustrated in Figure 12.

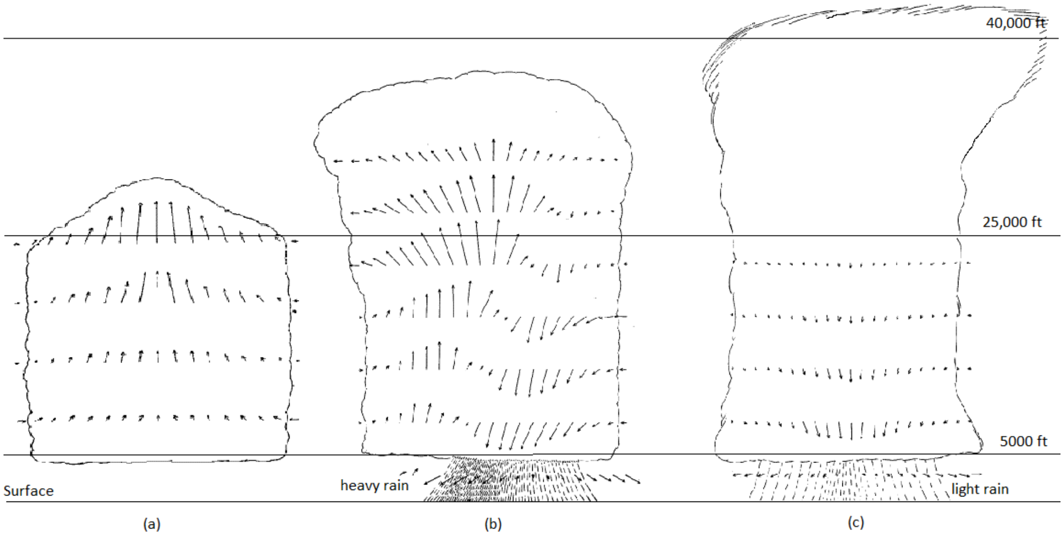

Figure 12. Illustration of the three stage life cycle of a typical airmass thunderstorm with the (a) cumulus, (b) mature, and (c) dissipating stages. Horizontal distance is not to scale. Adapted from Byers and Braham Jr. (1948).

2.1.2 Florida Airmass Thunderstorms.

The essential atmospheric requirements for thunderstorm development are significant amounts of low-level moisture, atmospheric instability, and upward vertical motion, often called "lift" (Biggar 1992). Lift, associated with typical airmass thunderstorms, is generally caused by thermally induced vertical motion from diurnal heating. This form of lift in an unstable airmass, when combined with sufficient moisture, can lead to thunderstorm development. However, the initial assumption that the majority of thunderstorm activity over Florida was caused only by airmass instability was determined to be invalid by Byers and Rodebush (1948). Instead, they found that thunderstorm development over Florida is often attributed to sea breeze convergence in conjunction with the thermally induced upward vertical motion due to diurnal heating (Byers and Rodebush 1948).

2.2 The Sea Breeze

The sea breeze is a local circulation that occurs during weak background synoptic forcing at coastal locations where, because of the low thermal conductivity of soil, land temperature responses to solar insolation are concentrated in a thin layer just below the surface which causes land surfaces to heat up more rapidly than the surrounding sea waters (Miller et al. 2003; Wallace and Hobbs 2006). During daytime heating the thermal contrast between land and water yields a local-scale pressure gradient force directed towards the land from the water which forces a shallow layer of moist air inland (Miller et al. 2003). The opposite of the sea breeze, the land breeze, occurs at night when the land cools quicker than the surrounding waters, and the pressure gradient reverses, thus driving an opposite circulation (Wallace and Hobbs 2006).

2.2.1 Sea Breeze Structure.

The sea breeze or sea breeze system has a structure of several specific components. As illustrated in Figure 13.

(a) The sea breeze circulation (SBC) is a vertically rotating mesoscale cell with flow at the surface directed toward the shore and return flow toward the sea (Miller et al. 2003). Rising air currents occur with inland flow while diffuse sinking currents occur several kilometers out to sea near 900 mb (Miller et al. 2003).

(b) The sea breeze gravity current (SBG) is the landward flow of moist, cool marine air in the lower horizontal arm of the sea breeze circulation (Miller et al. 2003).

(c) The sea breeze front (SBF) is the landward edge of the sea breeze gravity current and the sea breeze circulation, which can be associated with abrupt changes in temperature, moisture, and wind direction and speed (Miller et al. 2003). At times the approach of the sea breeze front is marked by fair-weather cumulus clouds (Cu), and in convectively unstable environments can trigger thunderstorms (Miller et al. 2003; Wallace and Hobbs 2006).

(d) The sea breeze head (SBH) is the raised head above and behind the sea breeze front which is created by updrafts from within both the continental and marine air masses, and is approximately twice as high as the following feeder flow behind the sea breeze front which reaches approximately 0.5 to 1 km thick (Miller et al. 2003; Wallace and Hobbs 2006).

(e) Kelvin-Helmholtz billows (KHBs) are the waves that develop along the upper boundary of the sea breeze gravity current which typically occur during midday because of low static stability (Miller et al. 2003). Wallace and Hobbs (2006) further explain that KHBs are produced by the presence of vertical wind shear at the density interface between the low level sea breeze and the return flow above. In addition KHBs increase the frictional drag on the sea breeze by entraining low momentum air from above the density interface (Wallace and Hobbs 2006).

(f) The convective internal boundary layer (CIBL) is the unstable region within the marine airmass which appears at the coast and grows in depth with distance inland and can often trap low-level pollutants (Miller et al. 2003). This is referred to as the thermal internal boundary layer (TIBL) by Wallace and Hobbs (2006) who also explain that its depth grows with the square root of distance from the shore as the marine air is modified by the heat flux from the warm land surface.

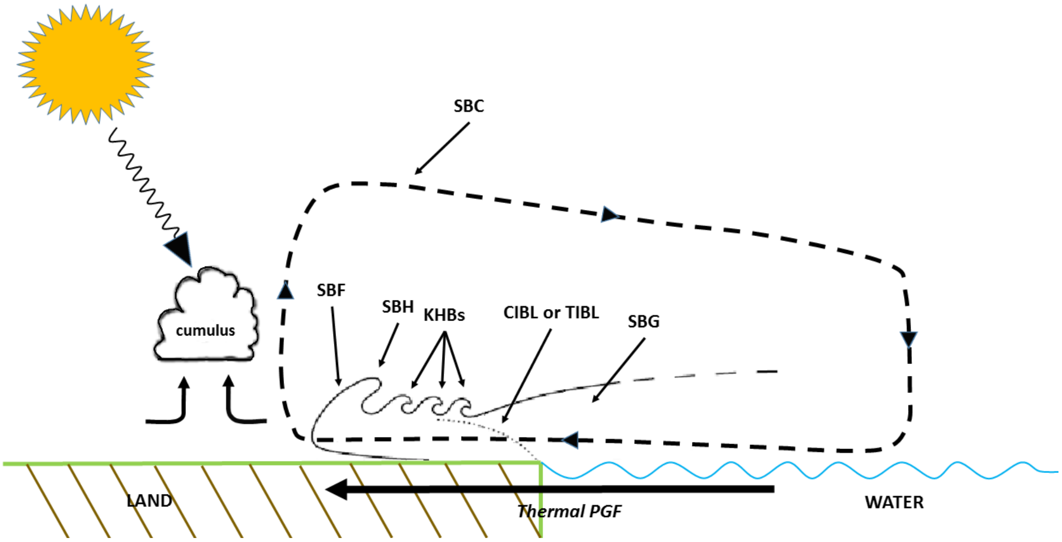

Figure 13. Illustration of specific components of the sea breeze system. Adapted from Miller et al. (2003).

2.2.2 Mathematical Representation.

In order to better conceptualize the physical mechanisms of the sea breeze circulation, a mathematical representation of the phenomenon can be utilized. One simplified mathematical approach is using the circulation theorem as presented by Holton and Hakim (2013). Mathematically, circulation about a closed contour in a fluid is defined as the line integral along the contour of the component of the velocity vector that is locally tangent to the contour (Holton and Hakim 2013). According to Holton and Hakim (2013), in a baroclinic fluid, where density depends on both temperature and pressure, circulation may be generated by the pressure-density solenoid term which is the right-hand side of the circulation theorem given by

$$\frac{D\,C_a}{Dt} = -\oint \frac{dP}{\rho}, \tag{1}$$

where $\frac{D}{Dt}$ is the total derivative or the material derivative, C_a is the circulation, P is pressure $[Pa]$, and ρ is density $[kg\ m^{-3}]$. As depicted in Figure 14, the mean temperature in the air over the ocean is colder than the mean temperature over the land, and consequently if the pressure is uniform at the ground level, the isobaric surfaces above the ground will slope downward toward the ocean, while the isopycnic surfaces, or surfaces of constant density, will slope downward toward the land (Holton and Hakim 2013). The theorem can be rewritten by using the ideal gas law,

$$P = \rho RT, \tag{2}$$

where T is temperature $[K]$ and R is the dry air gas constant ($287\ J\ kg^{-1}\ K^{-1}$) to substitute for ρ giving

$$\frac{D\,C_a}{Dt} = R\,ln(p_0/p_1)(\overline{T_2} - \overline{T_1}) > 0. \tag{3}$$

If follows that when letting $\overline{U}$ be the mean tangential velocity along the circuit the expression becomes

$$\frac{D\,\overline{U}}{Dt} = \frac{R\,ln(p_0/p_1)}{2(H+L)}(\overline{T_2} - \overline{T_1}). \tag{4}$$

As Holton and Hakim (2013) state, when letting $p_0 = 1000\ hPa$, $p_1 = 900\ hPa$, $\overline{T_2} - \overline{T_1} = 10°C$, $L = 20\ km$, and $H = 1\ km$, the acceleration computes to approximately $7 \times 10^{-3}\ m\ s^{-2}$. If assuming no frictional forces, this would produce a wind speed of $25\ m\,s^{-1}$ or about 48.6 knots in an hour. In reality, as the wind speed increases, frictional force reduces the acceleration and cool temperature advection from the sea to the land reduces the land-sea temperature contrast creating a balance between kinetic energy production from the pressure density solenoids and frictional dissipation (Holton and Hakim 2013). Miller et al. (2003) suggest that surface wind speeds of $6 - 7\ m\ s^{-1}$ can be reasonably expected.

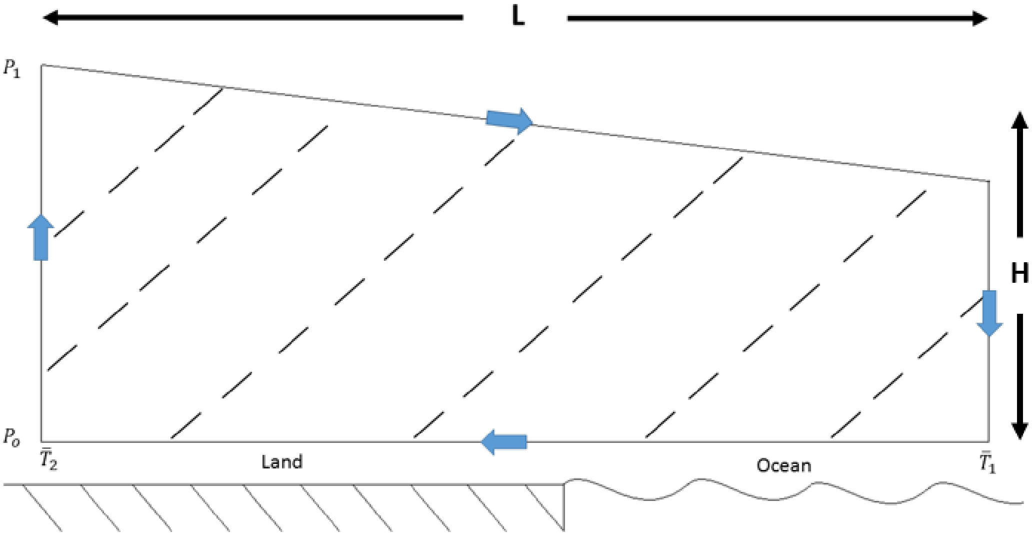

Figure 14. Illustration of the application of the circulation theorem to represent the sea breeze circulation based on the approach from Holton and Hakim (2013). Dashed lines indicate constant density surfaces. Depiction adapted from Holton and Hakim (2013).

2.3 Previous Sea Breeze Research

2.3.1 Sea Breeze Response to Synoptic-Scale Wind.

One of the main factors in sea breeze intensity is the condition of the synoptic-scale wind. Early research from Estoque (1962), using a hydrostatic model and the assumption of a straight shore, found specific sea breeze responses from large-scale, geostrophic winds. Specifically, offshore winds caused a much stronger sea breeze circulation than onshore winds due to the advection of warmer air which added to the horizontal temperature gradient, which increased the pressure gradient (Estoque 1962). Parallel flow also indicated changes to the pressure gradient. In the case of geostrophic wind along the shoreline with low pressure over the ocean, seaward frictional inflow increased the pressure gradient in the same manner as offshore wind, but with weaker effect Estoque (1962).

Bechtold et al. (1991) later used a two-dimensional non-linear model to research the effects of synoptic-scale flow by using varying magnitudes of wind flow. Bechtold et al. (1991) obtained similar results as Estoque (1962) in that offshore flow caused the strongest sea breeze circulations. Bechtold et al. (1991) also determined that offshore flow of 10 ms^{-1} suppressed the formation of a thermal gradient and moved the sea breeze circulation offshore.

Two-dimensional modeling from Arritt (1993) supported the same conclusions of synoptic flow effects as Estoque (1962) and Bechtold et al. (1991). Specifically, Arritt (1993) found that with onshore flow, convergence frontogenesis is suppressed while calm to moderate offshore flow allowed inland penetration of the sea breeze circulation and positive feedback to occur between convergence frontogenesis and the strength of the front. In the case of offshore flow, because the convergence zone was located over land where there is less stability, large vertical and horizontal velocities developed and promoted the strongest sea breeze circulations (Arritt 1993). The opposite was observed when strong offshore flow occurred. The sea breeze circulation had no inland penetration and thus remained over the waters where the environment was more statically stable (Arritt 1993).

Zhong and Takle (1993) also confirmed the same synoptic flow influences on the sea breeze using a three-dimensional mesoscale numerical model for the irregular coastline of the Kennedy Space Center in Cape Canaveral, Florida. However, they also determined that the complexities of inland rivers and lagoons helped to create low level convergence and strong vertical motions due to merging onshore sea breezes and offshore flow from inland water sources.

Observational research on synoptic flow influences on sea breezes also exists. Atkins and Wakimoto (1997) researched sea breeze front development using Doppler radar. Using radar reflectivity, a sea breeze front can be observed as a "thin line" which is the result of a "region of enhanced radar reflectivity in the optically clear boundary layer" (Atkins and Wakimoto 1997). There is debate on the physical reason for the region of enhanced reflectivity, but according to Atkins and Wakimoto (1997) there is evidence that the principal cause is scattering by insects. Using the radar observations of thin lines over Cape Canaveral, Florida, Atkins and Wakimoto (1997) observed sea breeze behavior that reinforced the findings from Estoque (1962), Bechtold et al. (1991), Arritt (1993), and Zhong and Takle (1993). The most prominent radar thin lines observed by Atkins and Wakimoto (1997) were during offshore flow days indicating enhanced convergence between the sea breeze and the synoptic flow. During days with parallel flow, a thin line was not observed until late afternoon when convergence was sufficient to cause the thin line to appear. On days with onshore flow, no thin line was ever detectable due to only weak convergence, but with all sea breeze cases, Atkins and Wakimoto (1997) observed gradients of virtual temperature and mixing ratio at the surface. The largest magnitude gradients were observed from offshore flow days and the smallest magnitude gradients from onshore days (Atkins and Wakimoto 1997).

2.3.2 Coastline Geometry Effects.

Coastline shape or geometry also has influences on the development of the sea breeze and the sea breeze front. Laird et al. (1995), in a study over Cape Canaveral, Florida, observed variations in the direction of the sea breeze near irregular coastlines. Laird et al. (1995) also observed that such irregular coastlines led to persistent zones of convergence within the sea breeze air mass and increased the depth of the sea breeze circulation which supported convection development.

Gilliam et al. (2004), in a sea breeze study over the North and South Carolina coastline, found a relationship between coastline shape to the development of sea breeze fronts. The influence of synoptic winds on the sea breeze circulation was similar to past studies. However, Gilliam et al. (2004) found that intricate coastline shapes caused the sea breeze fronts to move inland at irregular speeds and intensities due to the changing relation of the synoptic flow to the varying coastline.

Simulations from Baker et al. (2001) over Cape Canaveral, Florida also indicated coastline influences on the sea breeze. In the simulations, the heaviest precipitation was occurred near convex coastlines due to added low level convergence from sea breeze circulations. With concave coastlines, the opposite occurred since the resulting sea breeze circulations would orient winds away from each other causing divergence. In addition to the shape of the coastline, Baker et al. (2001) also observed that initial soil moisture influenced the timing and location of precipitation. The heaviest modeled precipitation areas occurred over initially moist soil or downwind of such areas (Baker et al. 2001). The reason for the enhanced precipitation was due to the increased convective instability over the moist soil areas. As evidence of this, calculated convective available potential energy (CAPE) was 21% higher over over moist soil compared to dry soil (Baker et al. 2001).

2.3.3 Eglin AFB and Florida Panhandle Sea Breeze Research.

Much of the research on sea breeze and sea breeze associated convection has been focused predominantly on the Florida peninsula. The Florida peninsula's unique shape creates ideal conditions for sea breeze fronts to develop on both the west and east coasts which can often collide in the afternoon hours creating an area of increased low level convergence and thunderstorm development over central Florida. Byers and Rodebush (1948) observed significantly less convergence over the Florida panhandle compared to the Florida peninsula. This observation is not surprising since the Florida panhandle has only one coast to initiate sea breeze circulation. However, with such a large difference between the Florida peninsula and panhandle, it is important to review studies completed over the panhandle. The following research provides insight into the sea breeze effects and associated convection over the Florida panhandle and Eglin AFB.

Biggar (1992) studied the pre-convective environments of summer thunderstorms over the Florida panhandle using observed 12 UTC upper air data and one kilometer resolution GOES satellite imagery every half hour. Days with “undisturbed” synoptic conditions were classified as having “strong”, “weak”, or “no” convection. No convection days had a tendency to have northerly wind components at all levels while weak and strong convection days typically had southerly wind components at the 850 mb level. Strong convective days typically had westerly components at 850 mb and below while low-level easterly winds generally suppressed convection. In addition to wind effects on sea breeze associated convection, Biggar (1992) also found some correlation between convective activity and thermodynamic parameters from upper air data at 12 UTC. Specifically, the best parameters to forecast convection were humidity between 500 and 700 mb and the Surface based Lifted Index (SLI). For strong convection days, the average relative humidity in the 500 to 700 mb layer was nearly 20% greater than days with no convection. Interestingly, humidity values for weak and strong convection were similar in range with moisture levels near the surface and 400 mb at 85% and 40% respectively (Biggar 1992).

Camp et al. (1998) used cloud-to-ground lightning data from 1989 to 1994 over the Florida panhandle and adjacent coastal waters to find a relationship between prevailing flow and thunderstorm activity during the warm season between 1 May and 31 October. The prevailing flow was determined by subdividing the low-level vector mean wind, from 1000-700 mb, into categories of coast parallel, onshore, and offshore. Camp et al. (1998) found that the distribution of lightning over the Florida panhandle was partly dependent upon the direction and speed of the prevailing low-level flow. Wind speeds of $2 - 5\ m\,s^{-1}$ were generally more conducive to lightning as compared to wind speeds exceeding $5\ m\ s^{-1}$ which suppressed thunderstorm formation by inhibiting sea breeze convergence. For every wind direction category with the exception of southerly flow, $2 - 5\ m\,s^{-1}$ flow had a larger number of median lightning flashes. Wind direction was observed to be associated with differences in the moisture and stability of the environment. Particularly, with strong northeasterly flow, the environment was the driest and the most stable while southerly flow was the most humid and unstable.

Weaver (2006) completed a sea breeze front study for Eglin AFB and its range complex that involved 509 sea breeze days collected between May and September of 2001 to 2005. Propagation and intensity of the sea breeze front was studied for offshore, onshore, coast parallel easterly, and coast parallel westerly synoptic scale flow regimes. Initially, Weaver (2006) assumed that the coastline south of Eglin AFB was concave, but analysis helped determine that the northern coastline of the Choctawatchee Bay was actually the effective coastline for the area. This determination is made more plausible when observing the sea breeze develop under light synoptic-scale flow. The sea breeze, under such conditions, begins as a southeasterly wind which coincides with the orientation of the Choctawatchee bay coastline (Weaver 2006).

In regards to days with offshore wind flow, Weaver (2006) found that the inland penetration of the sea breeze was delayed by as much two hours as compared to onshore wind flow. On average, the start time for the sea breeze with offshore initiated flow was 1730 UTC. This caused the sea breeze front initially to be held at the coastline and kept cool marine air offshore while radiational heating was allowed to continue over the land. The combination of maximized convergence from offshore flow and the resulting strong thermal gradient contributed to the strength of the strongest sea breeze fronts. These sea breeze fronts would form from offshore wind speeds of $3-5\ m\ s^{-1}$ despite much of the previous numerical research indicating $5-6\ m\ s^{-1}$ was more conducive to the most intense sea breezes. For offshore flow greater than $9\ m\,s^{-1}$, no sea breeze formed along the coastline, but with offshore flow of $7-9\ m\,s^{-1}$ the sea breeze front was held to within 15 km of the coastline. Onshore flow, on the other hand, created weak sea breeze fronts that increased in strength late in the day. The average start time for onshore flow initiated sea breezes was 1330 UTC. Between 18 and 19 UTC, a weak sea breeze front would form 20 km inland. At this point during the day, turbulent mixing of the sea breeze air had decreased while convergence at the front had increased. The strongest sea breeze front observed with onshore flow was from $4\ m\ s^{-1}$ winds, but onshore flow greater than $5\ m\ s^{-1}$ suppressed sea breeze front development.

In addition to offshore and onshore flow, Weaver (2006) also observed distinct behavior for coast parallel easterly and westerly flow. For both parallel flows, sea breeze start time averaged to 1500 UTC. Sea breeze fronts initiating under coast parallel easterly flow were weaker than offshore initiated fronts, and sea breeze fronts initiating under coast parallel westerly flow were stronger than onshore initiated fronts and agrees with previous research and theory. Coast parallel easterly flow of $7-9\ m\,s^{-1}$ produced strong sea breeze fronts 20 km inland, but flow greater than $9\ m\,s^{-1}$ suppressed sea breeze development. Coast parallel westerly flow resulted in much stronger sea breeze fronts than parallel easterly flow. One of the strongest sea breeze fronts observed by Weaver (2006) formed from winds under $3-5\ m\,s^{-1}$ coast parallel westerly flow. The research from (Camp et al. 1998) agrees with this result since lightning flash density maxima were found along sections of the Florida panhandle under $2-5\ m\ s^{-1}$ westerly flow. Of particular note from Camp et al. (1998) is the region between East Bay and Choctawatchee Bay which can be seen in Figure 2. This area was a specific region of lightning flash maxima (Camp et al. 1998). A possible reason for this maxima can actually be seen in Figure 2, specfically along the water's edge between East Bay and Choctawatchee Bay. The coastline marked by the water's edge between the two bays is a convex coastline which would likely cause surface convergence over the western portion of the range complex, thus supporting the findings of Camp et al. (1998).

2.4 Previous Mesoscale and High Resolution Model Research

Pielke (1973) was one of the first to devote a three-dimensional model to study the sea breeze convergence and the associated convection over southern Florida. The model was a primitive equation model with 11 km spacing that included a boundary layer parameterization scheme that allowed for the representation of the initiation and evolution of the sea breeze circulation. The importance of this early model was that rather than only using two-dimensional models to study the sea breeze, Pielke (1973) could use modeling to take into account the asymmetries of the coast of south Florida as well as the influence of Lake Okeechobee. Using the model in several experiments, the influence of the synoptic wind flow as well as the shape of the coast proved to be very important in the initiation and evolution of the sea breeze. However, the final experiment involved the use of observed synoptic data as model input. The results indicated that the model predictions of moisture saturation matched well with shower and cumulonimbus locations. Pielke (1973) was able to determine from the model results that cumulonimbus complexes over south Florida, when under undisturbed conditions, are strongly influenced by the sea breeze circulation and that the sea breeze modifies the thermodynamics of the environment which causes any cumulus development to be strongly influenced.

Welsh et al. (1999) used the MM5 mesoscale numerical model to study its benefit to forecasting sea breeze initiated convection over the Northeast Florida and Southwest Georgia area. The study compared mesoscale numerical model simulations with data from the nearby WSR-88D Doppler radar and surface data from the Jacksonville Area Sea Breeze Experiment (JASBEX). The model in this study was a triple domain primitive-equation mesoscale model with grid point resolution of 36 km over the outer domain, 12 km over the middle domain, and 4 km over the innermost domain. The model also included non-hydrostatic dynamics, diffusion, a multi-level planetary boundary layer, surface friction, and the split, semi-implicit time-integration scheme. Overall, the model was found to do a “good job” in simulating convective activity offshore and inland, but the model was too slow in moving convective activity onshore in the study. Some of the other issues that Welsh et al. (1999) noticed were that the model did not represent key onshore features such as rivers and swamps, and the model resolution was not fine enough to resolve river breeze development. An important observation from Welsh et al. (1999) was that at the time of the study, modeling thunderstorm activity after initial onset was not yet a realistic goal due to the chaotic nature of convective processes and the required additional computational resources.

More recently Azorin-Molina et al. (2014) investigated sea breeze thunderstorms over the eastern Iberian Peninsula using experimental, high resolution versions of the European HIRLAM and HARMONIE models. The version of the HIRLAM used was a hydrostatic grid-point model while the HARMONIE was a non-hydrostatic spectral model. At the time of the research, the HIRLAM was employed as an operational numerical weather prediction system by nine weather agencies or services. The HARMONIE would be implemented shortly later as the operational numerical weather prediction system by most European weather services. The experimental HIRLAM was used with 5 km and 2.5 km grid spacing while the HARMONIE was used with 2.5 km grid spacing. The study focused on 15 deep convective sea breeze thunderstorms that were missed by the operational HIRLAM. The models' forecast performance was determined by comparing forecast values of precipitation to high-density gridded rain gauge measurements.

The 5 km HIRLAM predicted light to moderate precipitation which was weaker than observed at a displaced location while the 2.5 km HIRLAM predicted excessive amounts of rainfall for too large of an area. The 2.5 km HARMONIE, however, was able to predict the precipitation in the correct location with reasonable accuracy precipitation amount. It was reasoned by Azorin-Molina et al. (2014) that the coarse resolution of the 5 km HIRLAM was insufficient to resolve the sea breeze circulation and the resulting local winds. Additionally, underdeveloped physics caused issues. Specifically, the 2.5 km HIRLAM's overestimation bias was reasoned as being partly due to the model's assumption of precipitation fall speed of infinity, which in other words caused that precipitation to be placed on to the ground directly (Azorin-Molina et al. 2014). Thus, because the 2.5 km HARMONIE was composed of better developed physics and high horizontal resolution, it produced the most accurate sea breeze thunderstorm forecast.

2.5 Previous WINNDEX Research

An Air Force study by Cornell (1993) was conducted to compare the performance of WINNDEX to the actual occurrence of airmass thunderstorms during the warm seasons — May to September — from 1986 - 1990. The study verified WINNDEX forecasts for the main Eglin base area and the Eglin land range. Forecasts for the main Eglin base area were verified by the official Eglin surface observation when it reported rain, rain shower, or thunderstorm and/or a lighting strike occurred within 5 NM (nautical miles) of 30° 29'N and 86° 32'W. Verification for the Eglin Range was based on either Eglin or Hurlburt Field surface observations and lightning strikes within an area defined by 30° 45'N, 86° 55'W, and 30° 20'N, 86° 05'W. Cornell (1993) considered verification two ways: first, the occurrence or nonoccurrence of convective activity during the day, and second, the timing of the onset of that convective activity. Percent correct forecasts, probability of detection (POD), false alarm rate (FAR), the Heidke skill score (HSS), and the discriminant "V" scores were calculated to determine WINNDEX forecast score. The results in Table 1 show the skill results from all 706 days of the study by Cornell (1993).

Table 1. WINNDEX forecast study results from Cornell (1993). Results include percent correct forecast, probability of detection (POD), false alarm rate (FAR), Heidke skill score (HSS), and Hanssen and Kuipers' discriminant "V" score for WINNDEX Yes/No categorical forecasts for the Eglin range and main Eglin base area. Table adapted from Cornell (1993).

Cornell (1993) WINNDEX Study Results				
	Eglin Range		Eglin Main	
	Surface Report & Lightning	Lightning Only	Surface Report & Lightning	Lightning Only
% Correct	68	64	65	56
POD	77	77	70	72
FAR	21	31	26	56
HSS	.21	.18	.26	.17
V	.22	.18	.27	.19

2.6 High Resolution Rapid Refresh Model

For this study, output from the operational High Resolution Rapid Refresh (HRRR) model was utilized. The HRRR model is a 3 *km* resolution, hourly updating numerical weather prediction model that produces forecasts out to 15 hours (Benjamin et al. 2015). It contains 1799 by 1059 grid points with 50 vertical levels (Benjamin et al. 2015). The specific model version of the HRRR used in this study was implemented at the National Centers of Environmental Prediction (NCEP) on 30 September 2014 and uses version 3.4.1+ of the Weather Research and Forecasting (WRF) model with the Advanced Research WRF dynamical core or WRF-ARW v3.4.1+ for short (Benjamin et al. 2015).

2.6.1 Model Domain.

As indicated in Figure 15, the HRRR domain covers the continental United States (CONUS). The lateral boundary and initial conditions of the HRRR are taken from the Rapid Refresh (RAP) model which has a domain that covers all of North America with a 13 *km* grid point resolution (Benjamin et al. 2015). Similar to the HRRR, the RAP model is also an hourly updated model, but produces forecasts out to 18 hours. Boundary conditions for the RAP are obtained from the Global Forecast System (GFS) which is a global spectral model produced by NCEP with the ability to forecast out to 16 days with resolution of approximately 28 *km* for the first 7 days and approximately 70 *km* for forecasts afterwards (Benjamin et al. 2015; NCEI 2015).

2.6.2 Data Assimilation and Forecast Cycle.

As is done with all operational numerical weather prediction models, the HRRR model assimilates observed weather data. Table 2 provides a comprehensive list of the observations assimilated both in the RAP and HRRR models.

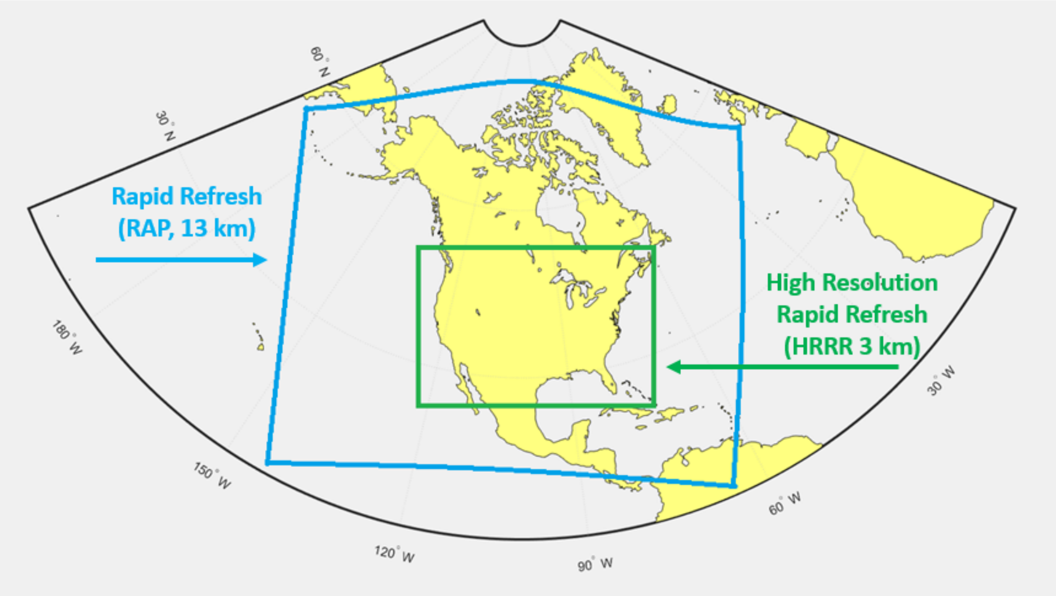

Figure 15. HRRR and RAP model domains (boundaries are not exact). Adapted from Benjamin et al. (2015).

In order to provide an overview of the HRRR forecast cycle, the RAP forecast cycle must first be addressed. The RAP forecast cycle begins with the previous model run's one hour forecast. The RAP then undergoes data assimilation which includes radar reflectivity data (Benjamin et al. 2015). After data assimilation, the model is run to produce an 18 hour forecast with the new one hour forecast used to initialize the data assimilation for the next forecast hour as illustrated in Figure 16. This process is repeated every hour each day.

The HRRR forecast cycle begins by interpolating the 13 *km* RAP data to 3 *km* (Benjamin et al. 2015). The HRRR model then undergoes a one hour "pre-forecast" period during which radar reflectivity data is assimilated in 15 minute increments until the model reaches the time of the next hour. At this point, the model undergoes data assimilation for the model 0 hour and is run to produce a 15 hour forecast (Benjamin et al., 2015). An illustration for this process is also provided in Figure 16.

Table 2. Hourly observations assimilated into both RAP and HRRR models. Adapted from Benjamin et al. (2015).

<table>
<tr><th colspan="3">Observations Assimilated into HRRR and RAP (Benjamin et al. 2015)</th></tr>
<tr><th>Hourly Observation Type</th><th>Variables Observed</th><th>Observation Count</th></tr>
<tr><td>Rawinsonde</td><td>Temperature, Humidity, Wind, & Pressure</td><td>120</td></tr>
<tr><td>Profiler/NOAA Network</td><td>Wind</td><td>Down to 9</td></tr>
<tr><td>Profiler - 915 MHz</td><td>Wind & Virtual Temperature</td><td>20 - 30</td></tr>
<tr><td>Radar VAD</td><td>Wind</td><td>125</td></tr>
<tr><td>CONUS Radar reflectivity</td><td>Rain, Snow, Hail</td><td>1,500,000</td></tr>
<tr><td>Aircraft/AMDAR</td><td>Wind & Temperature</td><td>2,000 - 15,000</td></tr>
<tr><td>Aircraft WVSS</td><td>Humidity</td><td>0 - 800</td></tr>
<tr><td>Surface/METAR</td><td>Moisture, Wind, Pressure, Clouds, Visibility, & Weather</td><td>2200 - 2500</td></tr>
<tr><td>Buoys, ships</td><td>Wind & Pressure</td><td>200 - 400</td></tr>
<tr><td>GOES AMVs</td><td>Wind</td><td>2000 - 4000</td></tr>
<tr><td>AMSU, HIRS, MHS</td><td>Radiances</td><td>5,000</td></tr>
<tr><td>GOES cloud-top press/temp</td><td>Cloud Top Height</td><td>100,000</td></tr>
<tr><td>GPS Precipitable water</td><td>Humidity</td><td>260</td></tr>
<tr><td>WindSat Scatterometer</td><td>Winds</td><td>2,000 - 10,000</td></tr>
</table>

2.6.3 Model Physics and Assumptions.

The HRRR and RAP both utilize the WRF-ARW which contains specific radiation, boundary layer, land-surface, and microphysics parameterizations. The following briefly discusses the physics schemes and model assumptions important to the uniqueness of the HRRR.

2.6.3.1 Land Surface Model.

The land surface model (LSM) used in the HRRR and the RAP is unique for several reasons. First, the LSM contains nine soil levels: 0, 1, 4, 10, 30, 60, 100, 160, and 300 *cm* (Benjamin et al. 2015). Having this larger number of soil levels pro-

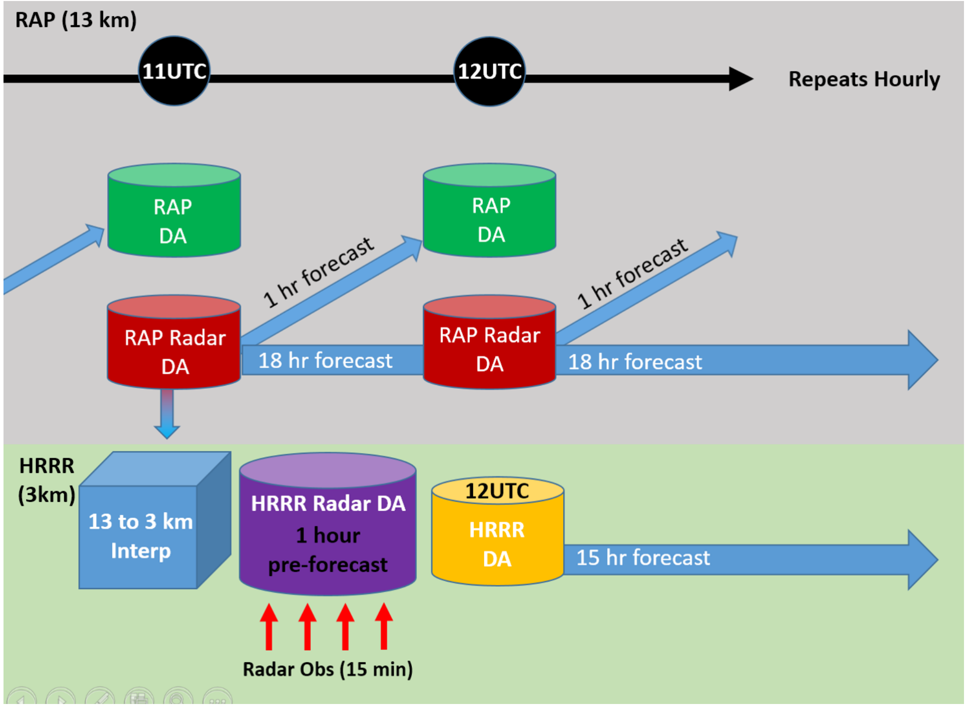

Figure 16. Illustration of RAP and HRRR forecast cycles. Adapted from Benjamin et al. (2015).

vides a more accurate representation of the diurnal soil cycle (Benjamin et al. 2015). The LSM fields are also cycled from one model run to the next which allows model precipitation to impact the soil state in future model runs (Benjamin et al. 2015). Additionally, surface observations are incorporated into the updates for the LSM. This allows soil temperature and moisture updates derived from surface temperatures and dew point observations (Benjamin et al. 2015).

2.6.3.2 Microphysics.

The Thompson Microphysics Scheme used in the both the HRRR and RAP contains two cloud hydrometeor and three precipitation hydrometeor types. The cloud hydrometeors include cloud water and cloud ice, while the precipitation hydrometeors contain rain, snow, and graupel which specifically encompasses all ice precipitation particles to include hail (Benjamin et al. 2015).

2.6.3.3 Convective Parameterization.

In most numerical weather prediction models, convective parameterization is required to simulate convection. Convective parameterization is a way to represent the physical processes and effects that occur from deep moisture convection, such as in rain showers and thunderstorms (Benjamin et al. 2015). Because the grid scale of rain showers and thunderstorms are of the same magnitude of grid spacing in models such as the RAP, all the processes that contribute to the vertical redistribution of heat and moisture cannot be modeled by such coarse resolution models without convective parameterization (Benjamin et al. 2015). However, with 3 km horizontal grid spacing within the HRRR, convective parameterization is not required. The HRRR instead uses explicit convection which essentially implies that the HRRR utilizes the microphysics scheme at the grid-scale level. According to Benjamin et al. (2015), higher resolution models — at or below 4 km — explicit convection promotes more accuracy in storm structure, such as the development of individual storm cells or lines of storms.

2.6.3.4 Radar Reflectivity Assimilation Assumptions.

When the HRRR assimilates radar reflectivity during the one hour pre-forecast time period, different latent heating rates are assumed based on dBZ values from the assimilated reflectivity in order to promote convective circulations and precipitation in the model prior to the initial zero hour time of the model (Benjamin et al. 2015). The unit dBZ is defined by

$$dBZ = 10\log_{10}\frac{Z}{1\ mm^6/m^3}$$

where reflectivity factor or Z is proportional to the sum of the sixth power of the diameter (D) of all scattering targets in a sample volume (UCAR 2012). In equation form, Z is written as:

$$Z = \sum_{i=1}^{n} D_i^6$$

where the units for Z are mm^6/m^3 (UCAR 2012). During the one hour pre-forecast, reflectivity observations are input at 15-minute intervals. For each reflectivity observation, the required latent heating rate is specified for the previous 15-minute period (Benjamin et al. 2015). Four different situations with respect to observed reflectivity determine the heating rate that is assumed during the pre-forecast period. The first is an observed reflectivity less than or equal to 0 dBZ. In this case, a zero heating rate is assumed to suppress erroneous model precipitation. The second situation is when observed reflectivity is greater than 0 dBZ but less than 28 dBZ. In this situation the model microphysics heating rate is left unchanged. The third case is when observed reflectivity is greater than or equal to 28 dBZ. In this case, a positive heating rate is assumed in order to promote convective development. Lastly, in the event the observed reflectivity is not available, such as in cases when terrain blocks radar beams, the model microphysics heating rate is once again left unchanged (Benjamin et al. 2015).

2.6.4 Model Output.

The HRRR has much of the same model output as many of the numerical prediction models currently in operational use, such as temperature, dew point, and heights for standard pressure levels, but the HRRR also produces some useful and unique output.

One type of output the HRRR produces are its reflectivity products which include: simulated composite reflectivity, simulated 1 km AGL (above ground level) reflectivity, and simulated 1 km AGL hourly maximum reflectivity. Simulated composite reflectivity is expressed in dBZ and represents the model prediction of how the observed composite reflectivity radar picture would appear at the valid time of the output (NCEP 2015). Significant focus will be devoted to composite reflectivity in this study. The simulated 1 km AGL reflectivity is a simulated base reflectivity prediction for 1 km above ground level while the simulated 1 km AGL hourly maximum reflectivity is a prediction providing the maximum value over the previous hour (NCEP 2015). Both the simulated 1 km AGL reflectivity and the simulated 1 km AGL hourly maximum reflectivity are also expressed in dBZ.

Another important output the HRRR produces are its hourly maximum products. These products include the simulated 1 km AGL hourly maximum reflectivity, but also includes lightning threat, updraft helicity, 10 m wind, updraft velocity, and downdraft velocity. Of particular interest in this study is the lightning threat output.

Lightning threat provides the rate of predicted lightning flashes expressed as the number of lightning flashes per square kilometer over a 5-minute period. However, it must be said that this output parameter represents the maximum lightning flash rate predicted by the HRRR over the previous hour (NCEP 2015).

2.6.5 Model Limitations.

The following explains known limitations of the HRRR model radar data assimilation, temperature biases, and precipitation biases as discussed in the National Weather Service's (NWS) online training for the HRRR model by Benjamin et al. (2015).

2.6.5.1 Radar Data Assimilation Limitations.

Radar data assimilation in the HRRR has several limitations. The first is that neither radial velocity data nor dual-polarization data is assimilated in the version of the HRRR used in this study (Benjamin et al. 2015). Also, high reflectivity observations that may include hail are assumed to be rain or snow in the model (Benjamin et al. 2015). Additionally, because the latent heating is tuned for mid-latitude convection, the assumptions do not provide enough heating for stratiform precipitation or warm-rain processes as observed in the tropics (Benjamin et al. 2015).

2.6.5.2 Temperature and Dew Point Biases.

The HRRR also has some known temperature and dew point biases. Figure 17 shows that based on 2 m temperature and dew point as a function of time of day, forecast length, and time of year, the HRRR has a daytime warm bias and a daytime dry bias from July to September.

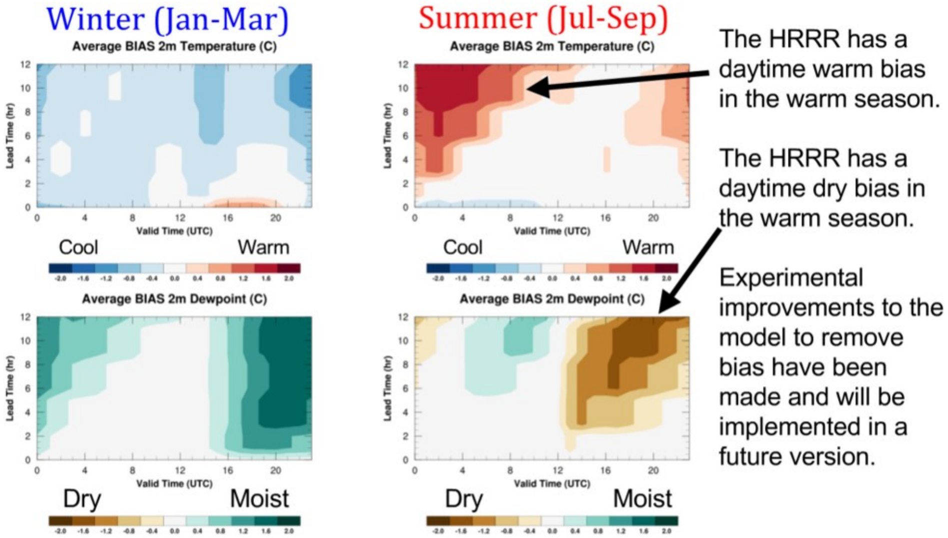

Winter (Jan-Mar)

Summer (Jul-Sep)

The HRRR has a daytime warm bias in the warm season.

The HRRR has a daytime dry bias in the warm season.

Experimental improvements to the model to remove bias have been made and will be implemented in a future version.

Figure 17. Two meter temperature and dew point biases as a function of time of day, forecast length, and time of year as illustrated by the NWS online training for the HRRR (Benjamin et al. 2015).

2.6.5.3 Precipitation Biases.

The HRRR also has some notable precipitation biases. In Figure 18, Benjamin et al. (2015) indicate the HRRR precipitation biases using the difference between the HRRR 6-hour forecasts and the NCEP Stage IV precipitation analysis from 1 June to 31 August 2013. The Stage IV precipitation analysis is the mosaic observed national product at NCEP that is derived from regional hourly and 6-hourly radar and rain gauge precipitation analyses produced by the 12 River Forecast Centers over CONUS (EMC 2015). Of specific concern in this study is the strong over-forecast of precipitation produced by the HRRR in the southeast United States, especially the Florida Panhandle area.

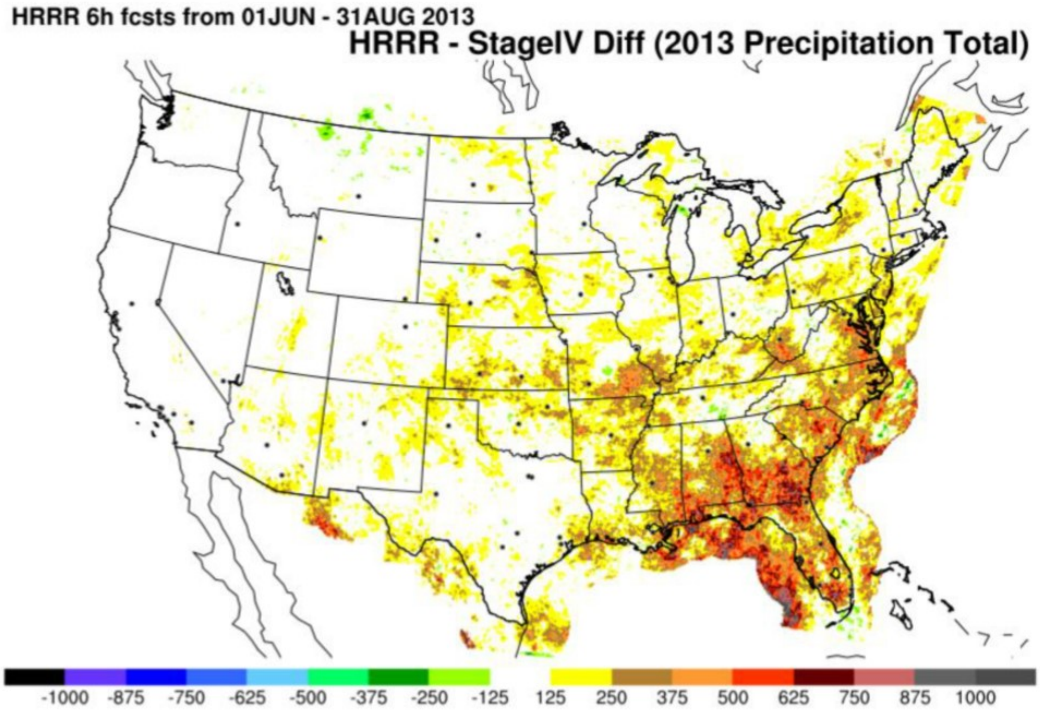

Figure 18. HRRR 6-hour precipitation difference from NCEP Stage IV precipitation analysis for the 2013 year from June through August plotted spatially over CONUS as illustrated by the NWS online training for the HRRR (Benjamin et al. 2015).

2.6.6 Reasoning for Using HRRR.

Despite its known limitations, the HRRR has shown possible skill when used by forecasters at Eglin AFB. The high resolution of the HRRR at 3 km can represent the Florida coastline better than other current operational models. There is also potential that environmental parameters, such as synoptic-scale winds, will be better represented. Additionally, because the HRRR is an easily accessed operational model, its use is both economical and operationally advantageous. It is for these reasons that the question of skill between WINNDEX and the HRRR should be investigated. The following chapter will discuss the methodology used to make this comparison.

III. Methodology

3.1 HRRR Model Data

The HRRR model data in this study was obtained from the NOAA Operational Model Archive and Distribution System (NOMADS) in GRIB2 (GRIdded Binary edition 2) files. HRRR GRIB2 files were downloaded from the NOMADS website using MATLAB® in order to automate the download process. Because of the large size of the model files, HRRR files are only available for 2 days. Consequently, each day required running a MATLAB® script to download each day's model data.

Two types of HRRR GRIB2 files were downloaded using the 12 UTC model run: surface and pressure files. The surface files contained all the output surface parameters from the model. All 16 hourly surface files were downloaded to obtain the data for lightning threat and simulated composite reflectivity for each hour. The pressure files contained parameters for the surface and 40 pressure levels above the surface. Unlike the surface files, only the 12 UTC pressure file was downloaded for each day since the data was only needed to provide inputs for WINNDEX.

HRRR GRIB2 files were downloaded from May through the end of September 2015 to cover the warm season over Eglin AFB. Because of initial coding errors, data did not successfully download until 8 May 2015 and during several days downloads were not completely successful either due to internet connectivity difficulties or possible issues with the NOMADS server. Days which had partially downloaded hourly files or missing files were omitted from the study. Despite the difficulties, a total of 136 days of HRRR model data were downloaded between 8 May and 30 September 2015.

3.1.1 Map Projection of Gridded Data.

Because HRRR GRIB2 files use x and y coordinates rather than latitude and longitude, it was required to convert the HRRR data coordinates before analysis. HRRR model data is organized in a 1799 by 1059 array with $3\,km$ grid spacing using a Lambert conformal conic projection with one standard parallel located at 38.5 degrees of latitude. Thus, using formulas from Snyder (1982), the x and y coordinates were converted to latitude and longitude values. Figure 19 provides two graphical plots for comparison of the two coordinate systems. The first plot uses x and y coordinates in 3 km units. The second plot uses latitude and longitude in degrees.

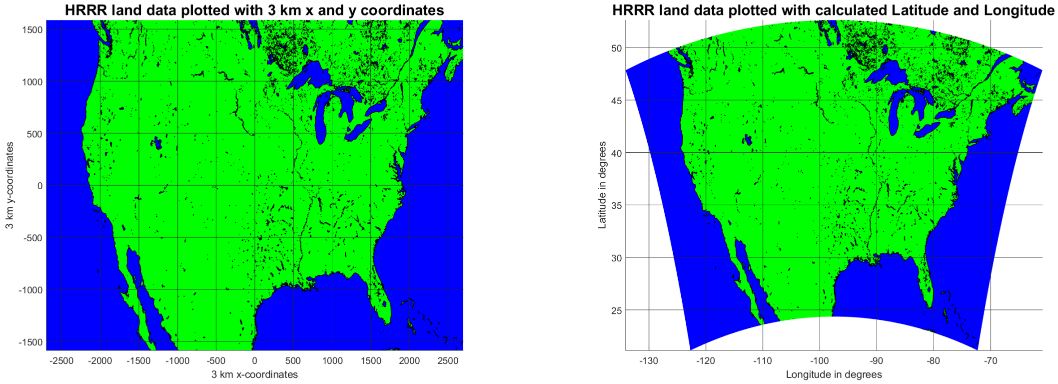

(a) HRRR plot with x and y coordinates

(b) HRRR land plot with latitude and longitude coordinates

Figure 19. Comparison plots of HRRR land data. (a) is plotted using x and y coordinates in 3 km units. (b) is plotted using latitude and longitude coordinates.

3.2 WINNDEX Input Data and Automation

In order to analyze forecast accuracy from WINNDEX, an automation of the WINNDEX process was developed using MATLAB®. The automation was designed to take 12 UTC HRRR model pressure fields and locate the closest grid point to the location of Eglin AFB. Using the model data from that grid point at multiple pressure levels, the CCL, dew point depression, and wind direction values required to use WINNDEX could be obtained for each day.

3.2.1 Reasoning for Using Model Data Versus Observed Soundings.

Before work started in this study, it was determined after discussion with staff meteorologists at Eglin AFB that it would be more appropriate to use the HRRR model data for sounding data instead of any observed soundings in the area. There were several reasons for this decision.

The first was the lack of a daily observed sounding at Eglin AFB. The weather flight at Eglin AFB does periodically launch a weather balloon to collect observed upper air data, but only when mission requirements dictate that the launch is necessary. The second reason was that any other soundings in the nearby area were too distant from Eglin AFB to provide accurate observation of the conditions over the base reliably on a daily basis. Instead, it was decided that the HRRR's high resolution output would provide the most accurate local upper air data for Eglin AFB in this study.

3.2.2 Digitization of Nomograms.

The first step in automating the WINNDEX process was digitizing the WINNDEX nomograms. Because the nomograms were designed as two-dimensional plots, x and y coordinate arrays were created in MATLAB® using its "meshgrid" function. Both x and y values were made to range from 0 to 60 in .05 increments. This range allowed for sufficient accuracy of sections within each nomogram while also not becoming so large that computation of the WINNDEX process required an unreasonable amount of time. This approach resulted in two coordinate arrays 1201 by 1201 in size.

With a coordinate system devised, the nomograms themselves needed to be converted into values that corresponded with the new coordinate system. To do this, each forecast section within each nomogram was denoted within a 1201 by 1201 array based on approximation of values from the hand drawn nomograms. Because the forecast sections in each nomogram are divided by lines, it was assumed that if x and y values fell on a line between sections, the section that would be selected would be the section that encompassed lower x and y values. This assumption allows the WINNDEX process to default to the more pessimistic forecast in the event values fall on a nomogram line. Graphical representations of the nomogram arrays are depicted in Figures 20 and 21. It should be evident that the digital plots closely follow the hand drawn plots from Figure 11.

3.2.3 Determining WINNDEX Input Values from HRRR Model Data.

With each nomogram represented in arrays, a MATLAB® script was then required to determine which nomogram to utilize and what x and y values to input to determine the WINNDEX forecast.

The script that was developed, as stated previously, determined the closest grid point to the location of Eglin AFB from the HRRR model data. Data from the 12 UTC pressure file corresponding to that grid point was used to provide the appropriate inputs into the WINNDEX process. The parameters used from the HRRR were geopotential height, temperature, dew point temperature, pressure, and wind speed. Wind speed was separated into two parameters, u and v which represent the zonal or easterly direction and the meridional or northerly direction, respectively.

3.2.3.1 Determining Wind Direction.

To determine the average wind direction at 12,000, 14,000, and 16,000 ft, a function was written to input the v wind speed and geopotential height and output the direction as either north or south. Geopotential height closest to 12,000, 14,000, and 16,000 ft were selected and their corresponding v wind speed values were averaged. If the average value was greater than or equal to zero, the output direction was classified

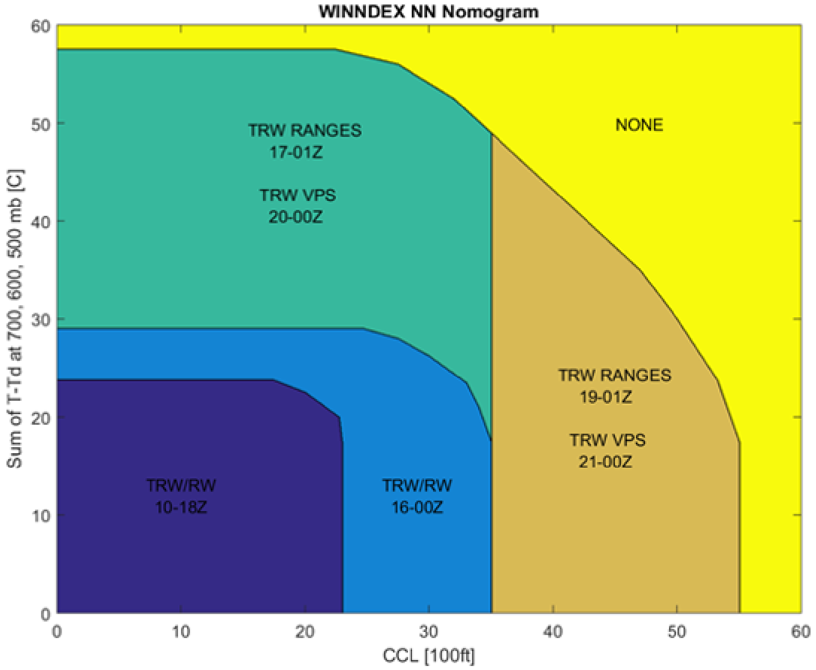

(a) Digitized nomogram for northerly 2000ft winds

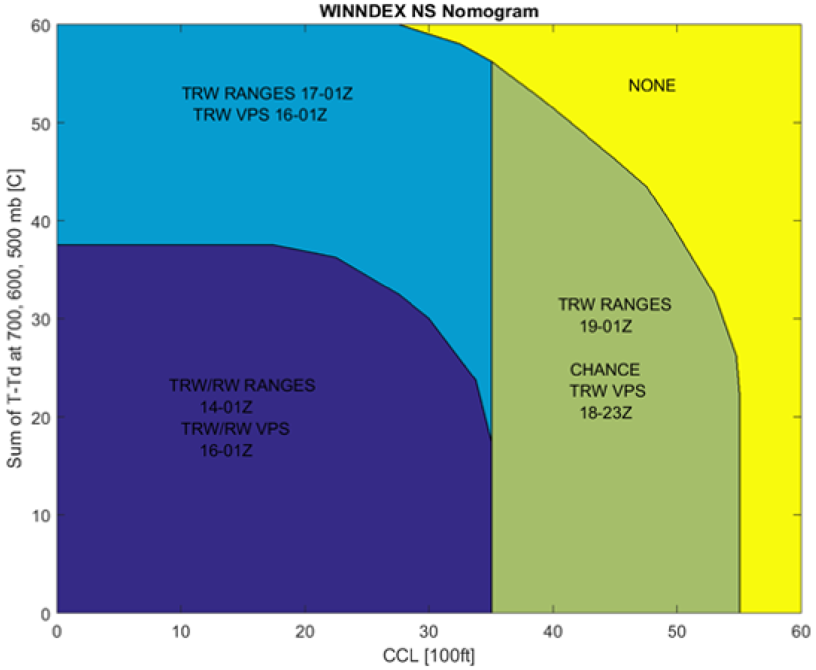

(b) Digitized nomogram for southerly 2000ft winds

Figure 20. Digitized WINNDEX Nomograms based on 1201 by 1201 arrays for upper level winds from the north.

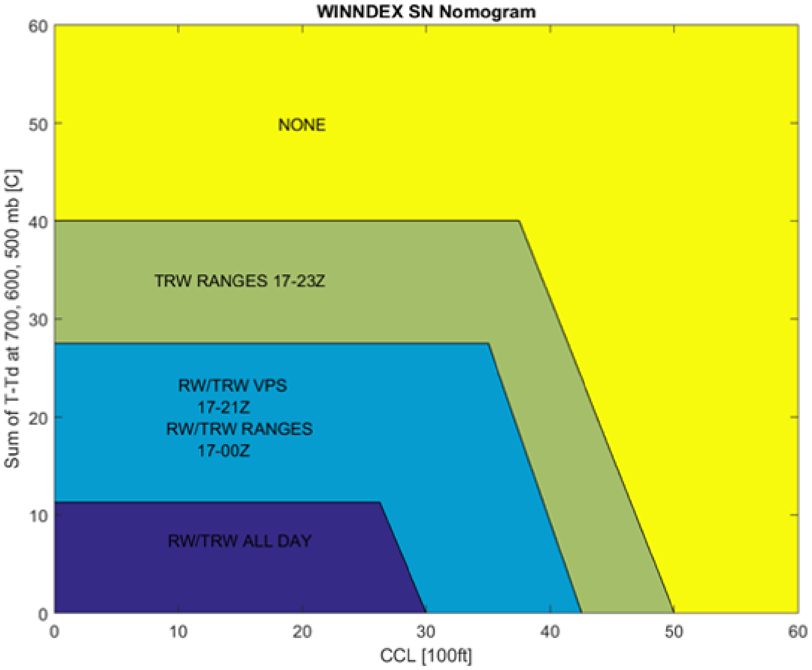

(a) Digitized nomogram for northerly 2000ft winds

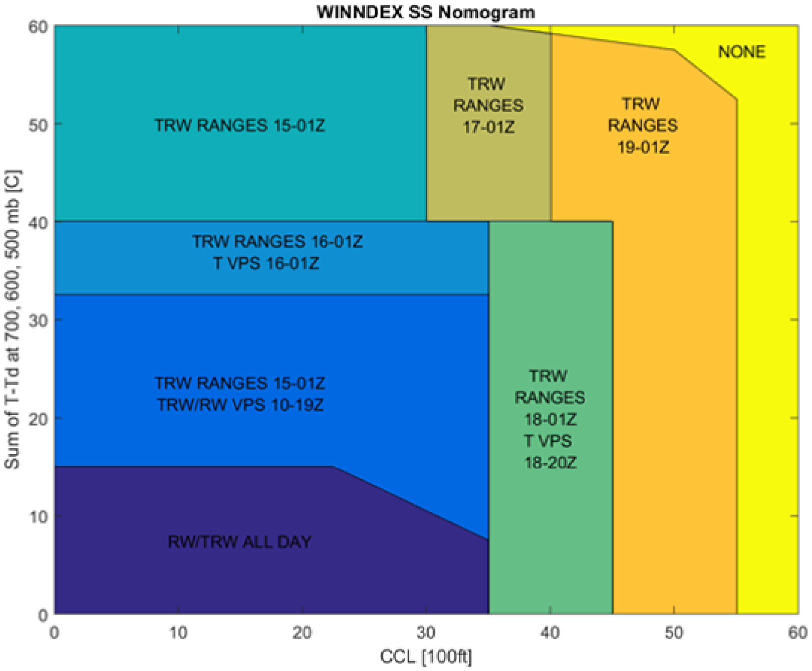

(b) Digitized nomogram for southerly 2000ft winds

Figure 21. Digitized WINNDEX Nomograms based on 1201 by 1201 arrays for upper level winds from the south.

as north. Conversely, if the average value was less than zero, the wind direction was classified as south. For wind direction at 2000 ft, the same process was performed with the exception of the requirement to average values. With determined wind directions for 2,000 ft and 12,000 through 16,000 ft, the appropriate nomogram for the wind conditions was selected.

3.2.3.2 Determining Sum of Dew Point Depression for 500, 600, and 700 mb Pressure Levels.

To determine the dew point depression sum, the process was simple with the use of the HRRR pressure file. The dew point temperature was subtracted from the temperature at 500, 600, and 700 mb levels and the values were then added together.

3.2.3.3 Determining Convective Condensation Level.

To determine the 12 UTC CCL for each day, a function was written to input geopotential height, pressure, temperature, and dew point temperature and output the CCL height. The calculations required two equations from Rogers and Yau (1996). The first equation is an empirical formula for vapor pressure which is defined as

$$e_s(T) = 6.112 \exp\left(\frac{17.67T}{T + 243.5}\right), \tag{5}$$

where e_s is in mb and T is in degrees C. The second equation is for mixing ratio which is defined as

$$w = \varepsilon \frac{e}{p - e} \tag{6}$$

where w is the mass of water vapor per unit mass of dry air, e is vapor pressure, and p is the total pressure. ε is R_d/R_v which is the ratio of the dry air constant and the individual gas constant for water vapor. R_d and R_v were set to equal 287 $Jkg^{-1}K^{-1}$ and 461.5 $Jkg^{-1}K^{-1}$ respectfully.

Because surface dew point temperature may not be completely representative of the amount of low level moisture in the atmosphere, the average mixing ratio from the lowest 50 mb of the atmosphere was used. This involved determining the dew point temperature from each level in the lowest 50 mb of the atmosphere. Using equations 5 and 6 and the dew point temperatures at each level, the mixing ratios were calculated and then averaged to determine the average mixing ratio from the lowest 50 mb.

The saturated mixing ratio at every level also needed to be calculated which also required equations 5 and 6, but required the temperature at each level rather than dew point temperature.

With both the average mixing ratio from the lowest 50 mb and the saturated mixing ratio at each level, the CCL height was determined by comparing the average mixing ratio to the saturated mixing ratio at each level. If the values equaled, then the height of the CCL was determined by the height of that particular level from the model data. However, if the average mixing ratio was greater than the saturated mixing ratio, then the CCL height was determined based on linear extrapolation between the previous level and level at which the average mixing ratio was greater than the saturated mixing ratio.

3.2.3.4 Inputting Values into Nomograms.

With the nomogram selected based on wind direction, and the height of CCL and dew point depression sum calculated, the WINNDEX forecast was determined by using the 1201 by 1201 coordinate arrays to locate the corresponding section value within the digitized nomogram. In order to ensure calculated x and y values always had a corresponding nomogram section, the values were rounded to the nearest .05. In addition, if any value was greater than 60, the forecast was assumed to be “none” for thunderstorms or rain showers.

3.3 HRRR and WINNDEX Verification

3.3.1 Verification Data.

Two types of observed verification data were used in this study. The first was archived lightning data which were provided by the 14th Weather Squadron. The second were archived composite radar reflectivity data downloaded from the National Centers for Environmental Information (NCEI) website, formerly the National Climatic Data Center (NCDC).

3.3.1.1 Filtered Days.

Because the sea breeze requires weak synoptic forcing, days which included squall lines or frontal boundaries were determined in order to complete analyses of forecast skill for both the entire warm season data set and a filtered data set. Thus, the filtered data set excluded those days on which synoptic conditions enabled convection by more than just interactions of diurnal heating and the sea breeze circulation. To determine days that had synoptic forcing, the archived surface analyses from the National Weather Services Weather Prediction Center website were used as seen in Figure 22.

3.3.1.2 Lightning Data.

The lightning data provided by the 14th Weather Squadron are archived data which was used in real-time operationally by the 557th Weather Wing, formerly the Air Force Weather Agency (AFWA). In February 2013, the then named AFWA

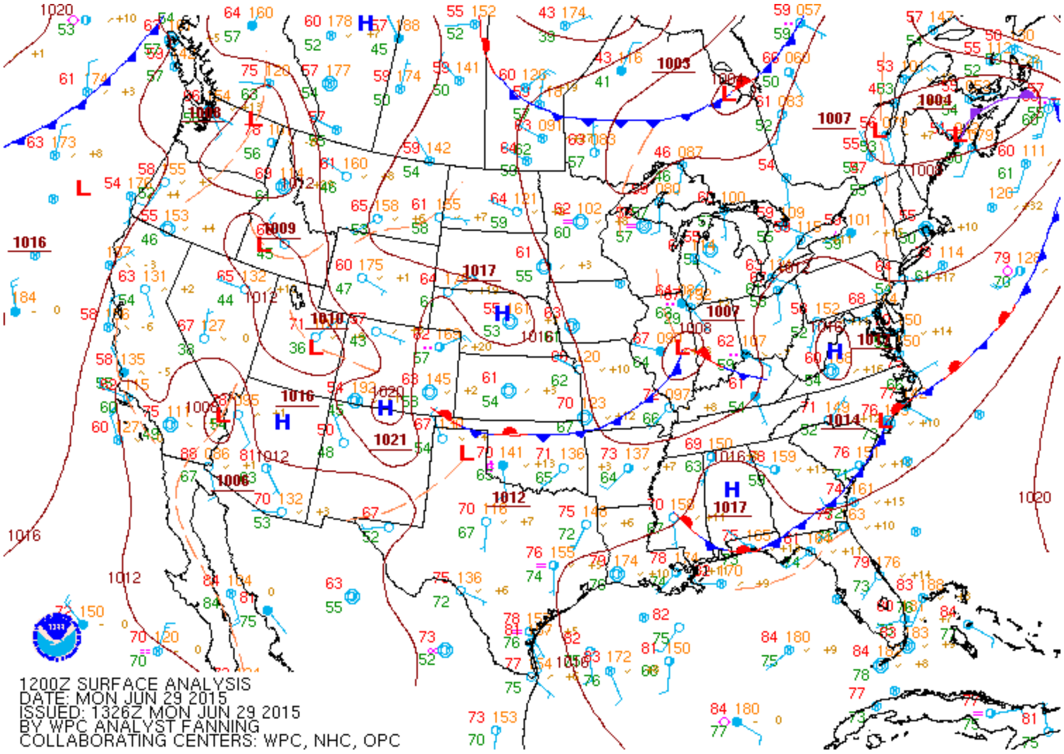

Figure 22. Example of surface analysis from the National Weather Services Weather Prediction Center website. In this analysis, a frontal boundary is clearly denoted over the western portion of the Florida Panhandle. Because the forcing on this day would not have been only attributed to the sea breeze circulation and environmental instability, this day would have been noted for filtered analysis.

changed its CONUS operational lightning data source from the National Lightning Detection Network (NLDN) to the Earth Networks Total Lightning Network (ENTLN) which is produced and operated by Earth Networks, Inc (Roeder 2013). Because the ENTLN is not as well known as the NLDN it is important to provide an overview of its capabilities and limitations, particularly when compared to the NLDN.

The main difference between ENTLN and NLDN is that ENTLN is considered to detect total lightning, which includes both lightning aloft, also known as cloud-to-cloud lightning, and cloud-to-ground lightning (Roeder 2013). NLDN, however, also detects cloud-to-ground lightning, but only detects lightning aloft at a much lower detection efficiency (Roeder 2013). Also, the ENTLN approaches lightning detection

Table 3. Comparison of Earth Networks Total Lightning Network (ENTLN) to the National Lightning Detection Network (NLDN). Adapted from Roeder (2013).

Comparison of ENTLN and NLDN as of April 2013		
	ENTLN	NLDN
Number of Sensors	550 (750 globally)	114
Detection Efficiency (CG-Ltg)	> 95%	> 95%
Median Location Accuracy (CG-Ltg)	300 m	250 m
Detects Cloud-to-Ground Lightning	Yes	Yes
Detects Lightning Aloft	Yes	No (survey level only)

differently than the NLDN. While the NLDN uses high performance sensors, the ENTLN uses lower cost and poorer performing sensors, but compensates by using many more sensors and advanced statistical processing (Roeder 2013). As a result, the overall performance of the ENTLN is comparable to the NLDN in CONUS. Table 3 provides key performance and attributes of the ENTLN and the NLDN based on data valid from April 2013. Figure 23 provides ENTLN CONUS sensor locations as of April 2013. It must be noted however, that both Earth Networks, Inc. and Vaisala, Inc. continue to add sensors and make improvements to their networks.

3.3.1.3 Composite Radar Reflectivity Data.

The composite reflectivity radar data downloaded from the NCEI website was specifically level-3 short-range composite reflectivity data. Three different radars within close proximity of Eglin AFB were used. The primary source was the KEVX radar, also known as the Eglin AFB radar, located at 30.564° latitude and −85.921° longitude which is 59 *km* east of Eglin AFB. The two other radars were the KEOX radar and the KMOB radars, known as the Fort Rucker and Mobile Regional Airport radars respectively. The KEOX radar is located at 31.460° latitude and −85.459° longitude, 149 *km* northeast of Eglin AFB. The KMOB radar is located at 30.679°

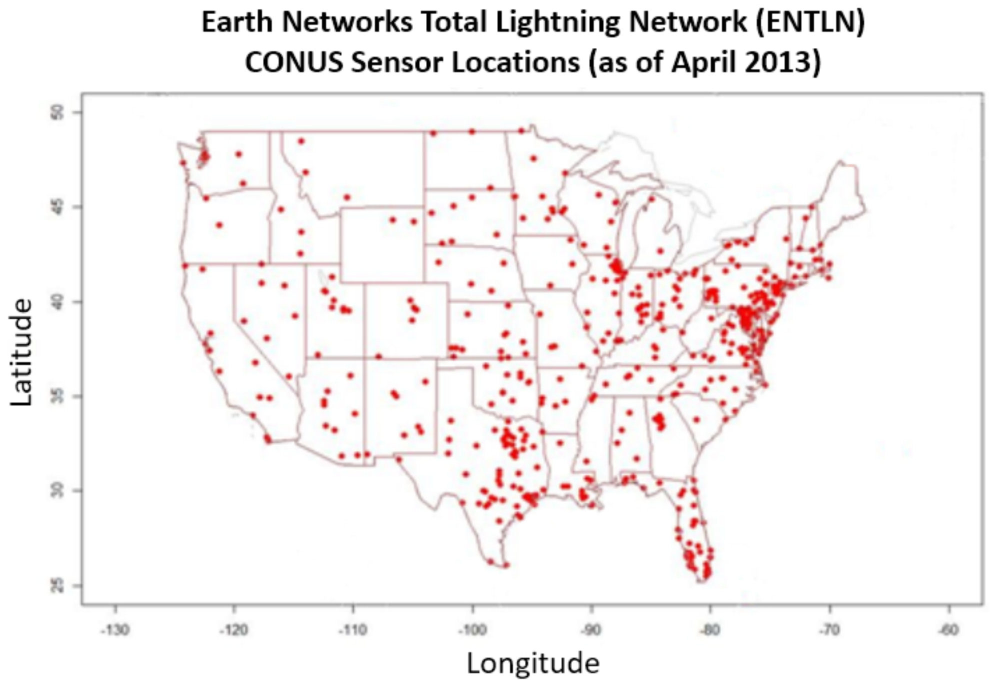

Figure 23. ENTLN CONUS sensor locations as of April 2013. Adapted from Roeder (2013).

latitude and $-88.239°$ longitude, 165 km west of Eglin AFB. Because the KEVX radar was not always operational during the study, radar data was used from KEOX and KMOB. In addition, due to KEOX being closer to Eglin AFB, KEOX data was used when KEVX data was unavailable, and when KEOX was not operational, the KMOB radar was utilized. With the combination of all three radars, each day in the study had complete radar coverage. Figure 24 illustrates the 230 km range coverage of all three radars and their positions relative to the Eglin AFB 5 NM range ring and the area used for verification for the Eglin range complex.

3.3.2 Verification Locations.

As mentioned above, Figure 24 indicates two locations around Eglin AFB, specfically the 5 NM range ring and the Eglin range complex. It is these two areas that have been used to verify the skill of both WINNDEX and the HRRR. The 5 NM ring

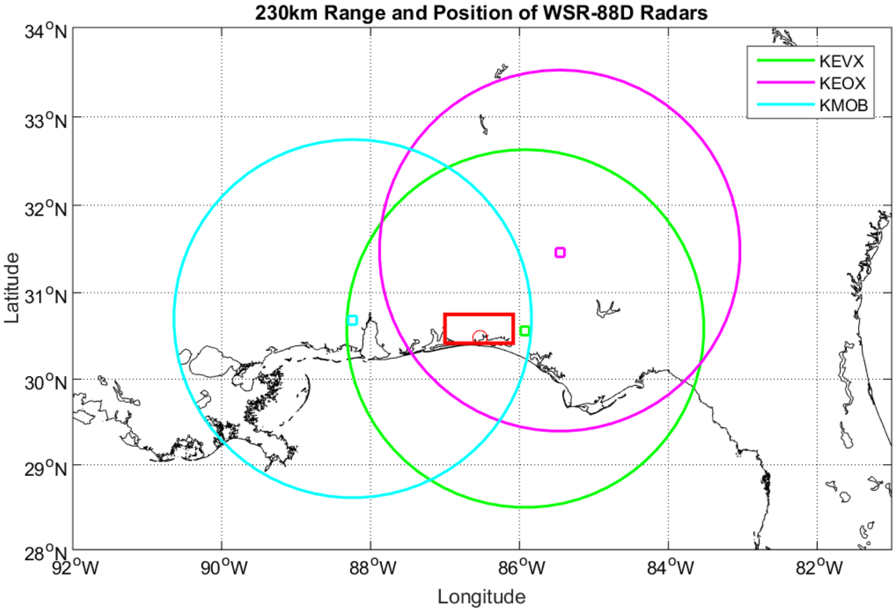

Figure 24. Radar coverage for KEVX, KEOX, and KMOB radars. The small, red ring represents the 5 NM range ring for Eglin AFB while the red box represents the area used for verification for the Eglin range complex.

is defined as a ring with a 5 NM radius centered at the point located at 30.48° latitude and −86.53° longitude. This ring also defines the terminal aerodrome forecast (TAF) area. The range perimeter is much more complex in shape and was represented by a box with four corners with the following coordinates: 1) 30.75° latitude and −87.00° longitude; 2) 30.75° latitude and −86.0833° longitude; 3)30.4166° latitude and −86.0833° longitude; 4) 30.4166° latitude and −86.00° longitude.

3.3.3 Verification Process.

In order to verify both the HRRR and WINNDEX forecasts the output from both at 12 UTC were compared. With the HRRR model forecasting 15 hours after initialization, the last forecast hour in this study is assumed to be 03 UTC. The last forecast hour from any WINNDEX nomogram is 01 UTC. Consequently hours after 01 UTC for WINNDEX were assumed to forecast for neither thunderstorms nor rain showers.

With regard to determining what determined a “yes” forecast or a “no” forecast for either thunderstorms or rain showers, for WINNDEX this was straightforward. If a nomogram section annotated that “TRW” or “RW” was to be forecast, then a “yes” forecast for rain showers was assumed for the time period indicated by that section. Similarly, for thunderstorm forecasts, if “TRW” or “T” was annotated in a nomogram section, then a “yes” forecast for lightning was assumed. For the HRRR model, determining a “yes” forecast involved establishing a threshold for the model outputs. In the case of lightning, any lightning threat value greater than zero was assumed to be a “yes” forecast for lightning. For composite reflectivity, a dBZ value of at least 30 was assumed to be a “yes” forecast for rain showers. Initially a value of 20 dBZ was used as the rain shower threshold due to literature indicating that the value is a reasonable point at which to expect precipitation. However, because each day in the archived radar data indicated at least 20 dBZ at some point in time within the Eglin range complex, the threshold was increased to 30 dBZ.

3.3.3.1 Lightning Verification.

Archived ENTLN lightning data was provided by the 14th Weather Squadron in comma separated value or .csv files. The values included lightning strike location in latitude and longitude coordinates, date of lightning strike, and time of lightning strike in hours, minutes, and seconds. Because both the HRRR and WINNDEX forecasts had hourly valid times, lightning strike time was considered using only hours and minutes. To distinguish between lightning strikes inside and outside of verification areas, a MATLAB® script was written to place a count of lightning strikes for each

HRRR grid point location for each forecast hour. Since the HRRR lightning threat parameter indicates a forecast for the maximum lightning flash rate from the previous hour, MATLAB® matrices that represented a particular forecast hour contained the lightning strike counts from the previous hour. The indices corresponding with the verification areas were then used for each lightning location matrix to provide the lightning strike counts of grid points within the verification areas. If the count was greater than zero within any grid point within a verification area, then it was assumed that lightning was observed within that area.

These lightning location matrices were used for hourly forecast verification of both the HRRR and WINNDEX forecasts. Daily verification, however, simply used the list of lightning strikes for each day. Strikes that had locations that did not occur within the coordinates of either verification area were eliminated and the first lightning strike that did occur within a verification area was saved with its time of occurrence. Thus for daily verification, the time of occurrence of the first observed lightning strike was all that was required to determine if lightning was observed.

3.3.3.2 Radar Verification.

Each composite reflectivity file downloaded contained a 464 by 464 array corresponding to radar dBZ values for a specific hour and minute. Each value in the 464 by 464 array represented a 1 *km* by 1 *km* grid point. In reality, the radar resolution decreases with distance from the radar. Consequently, the resolution of the archived radar data also appears to reduce in resolution at greater distances from the radar since the data contained in the 464 by 464 array is derived from radial radar data. In addition to the dBZ value array, the composite reflectivity files also contained the latitude and longitude values for the corners of the array based on a flat earth approximation. Thus, to calculate the latitude and longitude coordinates for each grid point in the array, latitude and longitude were linearly interpolated based on the size of the array and the values at each corner. With latitude and longitude coordinates, the verification areas could then be determined within the dBZ array.

For hourly verification, the closest radar file to the hourly forecast valid time for both HRRR and WINNDEX forecasts was determined. If a dBZ value of at least 30 dBZ was within a verification area, a rain shower was assumed to have occurred for that forecast hour. For daily verification, much like with lightning verification, the first radar file with a dBZ value of at least 30 within a verification area denoted a rain shower had occurred and the associated time was saved to calculate initial onset timing error.

3.4 Measures of Skill

3.4.1 2 x 2 Contingency Table.

Because the forecasts for both the HRRR and WINNDEX are discrete rather than probabilistic, a 2 x 2 contingency table was used to evaluate forecast skill and accuracy. Table 4 is a representation of the 2 x 2 contingency table used in this study. On the far left column are the labels for “Forecast Yes” and “Forecast No” while the labels on the top row are “Observed Yes” and “Observed No.” These labels correspond with the four values in the 2 x 2 table. “A”, “B”, “C”, and “D” represent the values in each cell. Wilks (2011) has outlined definitions for each value in the table in the following manner: the “A” value is defined as “hits”, the “B” value is defined as false alarms, the “C” value is defined as misses, and the “D” value can be defined as either “correct rejections or “correct negatives.” All the measures explained below, with the exception of timing error, use the values derived from the 2 x 2 contingency table. However, the reader is cautioned to closely notice the subtle differences the values of “B” and “C” take on when the forecast label column and the observed label row are switched. Cornell (1993) also used the 2 x 2 contingency table in his early study of WINNDEX forecast skill, however, his table did in fact switch the forecast and observed labels. Consequently, his equations for skill measures differ slightly. Thus, in this study, all equations for skill measures were taken from Wilks (2011) rather than from Cornell (1993). The only exception is the equation for false alarm rate which will be discussed more thoroughly below.

Table 4. Sample 2 x 2 contingency table adapted from Wilks (2011).

Sample 2 x 2 Contingency Table		
	Observed Yes	Observed No
Forecast Yes	(A) # of occurrences	(B) # of occurrences
Forecast No	(C) # of occurrences	(D) # of occurrences

3.4.2 Percent Correct.

The first skill measure, percent correct, is the most straightforward. Using the values outlined in Table 4, percent correct is defined by the following equation:

$$\%\ \text{Correct} = \frac{A + D}{A + B + C + D} \times 100. \tag{7}$$

As indicated by equation 7, percent correct is simply the percent form of the fraction of total forecasts that were correct (Wilks 2011). Percent correct credits correct “yes” and “no” forecasts equally and also penalizes both types of incorrect forecasts equally (Wilks 2011). This is a potential drawback since equal scoring between correct forecasts and incorrect forecasts can cause an undesirable indication of skill or lack of skill when either “yes” or “no” events are particularly rare (Wilks 2011). The best possible score is 100% while the worst possible score is 0%. The percent correct measure was used for both hourly and daily verification.

3.4.3 Probability of Detection.

Probability of detection (POD), also known as "hit rate" is a frequently used discrimination score (Wilks 2011). It is useful due to its ability to isolate the "event of interest" rather than include information about non-events (Wilks 2011). This compensates for the drawback of the percent correct measure for instances where there are a large amount of "no" events. POD is defined by the following equation:

$$\mathrm{POD} = \frac{A}{A+C} \times 100. \tag{8}$$

As indicated by equation 8, probability of detection is the percent form of the ratio of correct forecasts to the number of times the forecast event occurred (Wilks 2011). Just as in the case with the percent correct measure, the best possible score is 100% and the worst possible score is 0%. POD was used for both hourly and daily verification.

3.4.4 False Alarm Rate.

In this study the term, "False Alarm Rate" is taken from Cornell (1993), but the equation that has been used to define it is the percent form of the equation for false alarm ratio from Wilks (2011). The reason for this adaptation is the difference in 2 x 2 contingency table layouts between Cornell (1993) and Wilks (2011) as discussed earlier. In addition, Wilks (2011) has a separate equation and definition for "false alarm rate" which is not consistent with the Cornell (1993) definition of "false alarm rate." Thus, in order to maintain easy comparison to Cornell (1993), but at the same time alleviate confusion between sources, the following equation was used to define false alarm rate:

$$\mathrm{FAR} = \frac{B}{A+B} \times 100. \tag{9}$$

As indicated by equation 9, FAR is defined as the percent form of the ratio of "yes" forecasts that are verified as incorrect (Wilks 2011). FAR has a negative orientation which is to say that the best possible score is 0% and the worst possible score is 100% (Wilks 2011). FAR was used for both hourly and daily verification.

3.4.5 Bias.

Bias is the comparison of the average forecast with the average observation, but is represented as a ratio when used for verification of contingency tables (Wilks, 2011). Based on the terms in Table 4, the equation defining bias is:

$$\text{Bias} = \frac{A + B}{A + C}. \tag{10}$$

As equation 10 indicates, bias is the ratio of the number of "yes" forecasts to the number of "yes" observations. The most unbiased forecasts achieve a score of 1; however, scores greater or less than 1 are considered over-forecasting or under-forecasting respectively (Wilks 2011). It is important to note that the drawback to bias is that it does not provide information about the correspondence between forecasts and observations for specific occasions (Wilks 2011). Bias was used only for daily verification.

3.4.6 Critical Skill Index.

The critical skill index (CSI), also called "threat score", is an alternative to the percent correct measure and is particularly useful when "yes" events occur significantly less than "no" events (Wilks 2011). CSI is defined as:

$$\text{CSI} = \frac{A}{A + B + C}. \tag{11}$$

As indicated by equation 11, CSI is the ratio of correct "yes" forecasts to the total number of occasions the event was forecast and/or observed (Wilks 2011). The best possible score is 1 while the worst possible score is 0. CSI was used only for daily verification.

3.4.7 Heidke Skill Score.

The Heidke Skill Score, also used by Cornell (1993), uses a generic form for skill score. This form is characterized by a particular measure of accuracy with respect to the accuracy of a set of reference forecasts (Wilks 2011). The generic skill score form is given by:

$$\mathrm{SS} = \frac{A - A_{ref}}{A_{perf} - A_{ref}} \tag{12}$$

where A is the measure of accuracy, A_{ref} is the accuracy of a set of reference forecasts, and A_{perf} is the value of the accuracy measure that would be achieved by perfect forecasts. In the case of the Heidke Skill Score the reference accuracy measure is the proportion correct that would be achieved by random forecasts that are statistically independent of the observations (Wilks 2011). Using the values in Table 4, the probability of a "yes" forecast is given by $(A + B)/(n)$ and the probability of a "yes" observation is given by $(A + C)/(n)$ where n is equal to the total of all the values in the contingency table or simply $(A + B + C + D)$ (Wilks 2011).

When determining A_{ref} for Heidke Skill Score, it follows that the probability of a correct "yes" forecast by chance is

$$\frac{(A+B)}{n} \cdot \frac{(A+C)}{n} = \frac{(A+B)(A+C)}{n^2}, \tag{13}$$

and the probability of a correct “no” forecast by chance is

$$\frac{(B+D}{n} \cdot \frac{(C+D)}{n} = \frac{(B+D)(C+D)}{n^2}. \tag{14}$$

Subsequently, following equation 12, the Heidke Skill Score can then be written as

$$\mathrm{HSS} = \frac{(A+D)/n - [(A+B)(A+C)+(B+D)(C+D)]/n^2}{1-[(A+B)(A+C)+(B+D)(C+D)]/n^2} \tag{15}$$

which simplifies to

$$\mathrm{HSS} = \frac{2(AD-BC)}{(A+C)(C+D)+(A+B)(B+D)}. \tag{16}$$

Because the Heidke Skill Score uses the form of equation 12, it better reflects forecast skill as it is compared to random chance. Perfect forecasts achieve a score of 1, forecasts equal to the reference forecast achieve a zero, and forecasts worse than the reference forecasts receive a negative score. The Heidke Skill Score was used for daily verification only.

3.4.8 Peirce Skill Score.

The Peirce Skill Score (PSS), like the Heidke Skill Score, was also used by Cornell (1993), but was called by a different name — the Hanssen-Kuipers discriminant V. In order to remain consistent with Wilks (2011), the Peirce Skill Score name will be used here further. The Peirce Skill Score is formulated the same to the Heidke Skill Score with the exception of the reference hit rate in the denominator. This is to say that the random reference forecasts in the denominator have forecast probabilities that are equal to the observed probabilities. Or more simply, the reference accuracy in the denominator reflects the climatology of the sample used to calculate the score.

The Peirce Skill Score is then formulated as

$$\text{PSS} = \frac{(A + D)/n - [(A + B)(A + C) + (B + D)(C + D)]/n^2}{1 - [(A + C)^2 + (B + D)^2]/n^2}, \tag{17}$$

which simplifies to

$$\text{PSS} = \frac{(AD - BC)}{(A + C) + (B + D)}. \tag{18}$$

For Peirce Skill Score, perfect forecasts receive a score of 1, random forecasts receive a score of zero, and forecasts inferior to random forecasts receive negative scores (Wilks 2011). In addition, constant forecasts — forecasts that are always "yes" or always "no" — also receive a score of zero. An advantage of the Peirce Skill Score over the Heidke Skill Score is that the contribution to the Peirce Skill Score by a correct "no" or "yes" forecast actually increases as the event is more or less likely respectively (Wilks 2011). This enables forecasts to not be penalized for forecasting an event when the event has a low climatological probability of occurring (Wilks 2011). The Peirce Skill Score was used for daily verification only.

3.4.9 Timing Error.

Timing error is not technically a skill score, but it does still reflect "real world" accuracy of forecasts. In this study, timing error for the initial onset of lightning or rain showers as indicated by composite reflectivity was calculated by taking the initial time of occurrence for observed lightning or radar reflectivity and subtracting that time from HRRR and WINNDEX forecasts in minutes. This was done for each day that contained both an initial forecast time and an initial observed time. In equation form this can be written as T = F - O where F is the forecast time, O is the observed time, and T is timing error. Based on this simple equation, if the timing error is negative, then the forecast was early, and if the timing error is positive, then the forecast was late. If a forecast time or observed time was 00 UTC or later, 24 hours were added to the hourly value and then converted to minutes. Timing error was calculated for daily verification only.

IV. Results

4.1 Frequency of Observed and Forecast Occurrences

Before presenting hourly verification results, it is appropriate to provide the data for the frequency of observed and forecast occurrences for lightning and radar in order to better understand the context of the hourly verification results. Figure 25 provides the frequency of observed and forecast lightning for the range complex and the 5 NM ring while Figure 26 provides the frequency of observed and forecast rain showers (radar reflectivity exceeding 30 dBZ) also for the range complex and the 5 NM range ring.

The first noteworthy item with the frequency data is that, in general, the observed frequency follows the climatology data provided in Figure 10. However, the range complex has a much higher frequency of both lightning and radar occurrences as compared with the specific climatology for Eglin AFB in Figure 10. This is to be expected since the range complex is a much larger area than the 5 NM ring, and extends further inland. On the other hand, the observed frequency data for the 5 NM ring matches the base climatology more closely as can be seen when comparing the magnitude of values between the frequency data from Figures 25 (b) and 26 (b) to Figure 10.

The HRRR lightning forecast frequencies for the range generally over-forecast during periods outside of the peak thunderstorm occurrences between 19 - 22 UTC, but under-forecast during the period of peak thunderstorm occurrences. WINNDEX forecast frequencies exhibited the opposite behavior, over-forecasting during the period between 19 and 01 UTC and under-forecasting outside of that period.

For lightning forecast frequencies for the 5 NM ring in Figure 25(b), the HRRR managed to achieve relatively low bias during early hours, between 12 and 21 UTC, but over-forecast in later hours. WINNDEX, however, generally under-forecast in the period prior to 20 UTC and over-forecast between 21 and 00 UTC with a particularly high over-forecast bias.

Rain shower forecast frequencies for both the range and ring in Figure 26 indicated a general under-forecast bias for HRRR and WINNDEX with WINNDEX having the worst bias in the early hours. Specifically with WINNDEX, an interesting observation is that it achieved a more realistic diurnal variation for the 5 NM ring as compared to the range complex. Considering the fact that WINNDEX was developed 30 years ago when manual observations at Eglin AFB were relied upon more heavily and doppler radar was not yet prevalent, better diurnal accuracy specifically for the 5 NM ring makes sense.

Lastly, in regard to the frequency data, the hours before and after the majority of the occurrences, prior to 17 UTC and after 23 UTC, contained significantly lower frequencies than the rest of the data. This important attribute must be considered when analyzing the results for hourly verification.

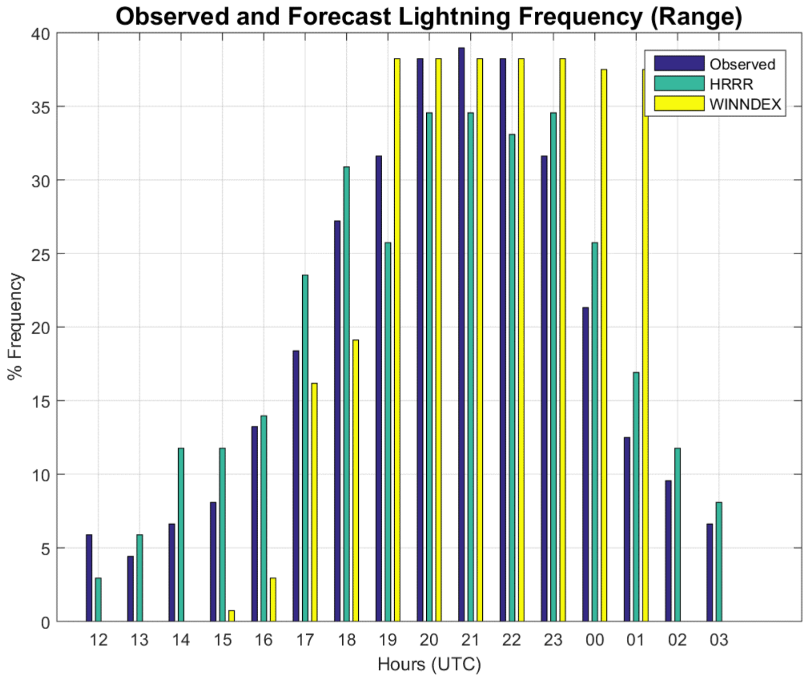

(a) Observed and forecast lightning frequency for the range complex.

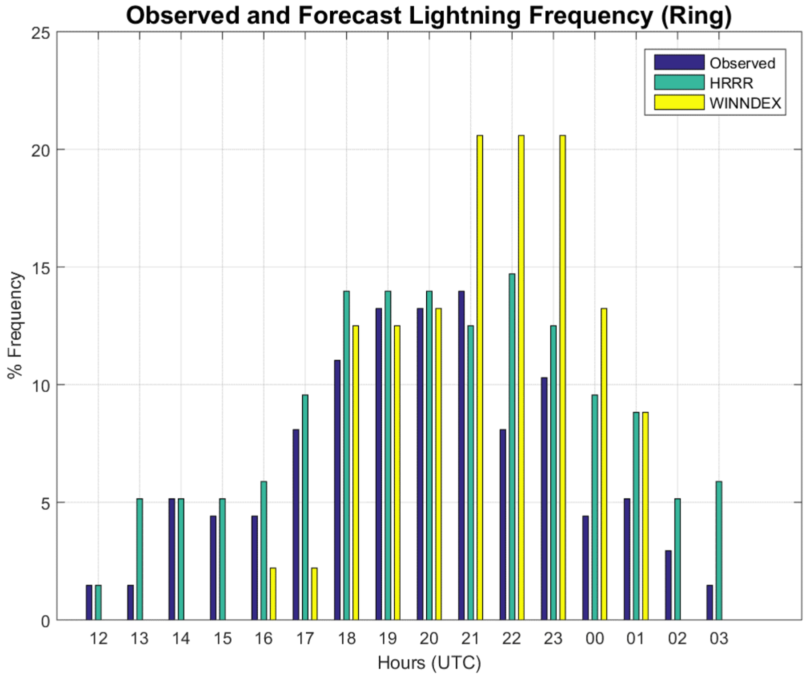

(b) Observed and forecast lightning frequency for the 5 NM range ring.

Figure 25. Observed and forecast lightning frequency for (a) the range complex and (b) the 5 NM ring.

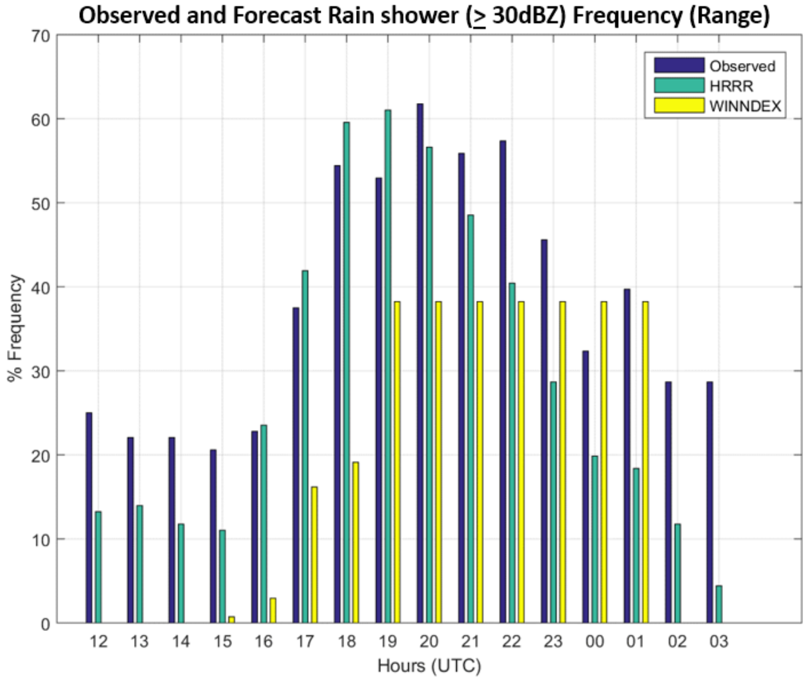

(a) Observed and forecast rain shower frequency for the range complex.

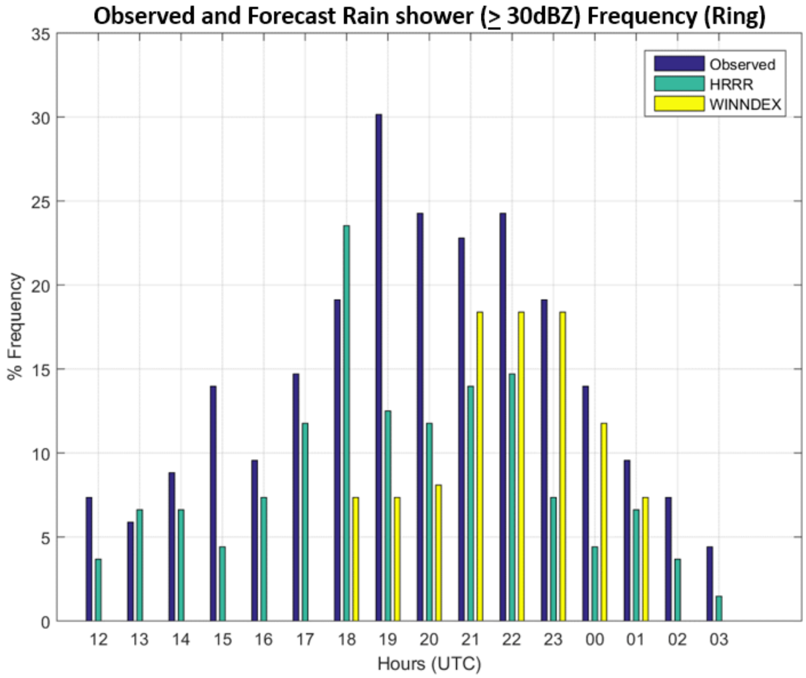

(b) Observed and forecast rain shower frequency for the 5 NM range ring.

Figure 26. Observed and forecast rain shower frequency for (a) the range complex and (b) the 5 NM ring.

4.2 Hourly Verification Results

Figures 27, 28, and 29 provide the hourly verification results for lightning and rain showers for both the HRRR and WINNDEX. Overall, hourly verification results indicate that the HRRR is more accurate than WINNDEX. The HRRR generally, especially in earlier forecast hours, has higher percent correct and probability of detection measures and lower false alarm rates for both lightning and rain showers.

In more detailed analysis, the most obvious attribute of the results is the higher skill for the range as compared to the 5 NM ring. This was expected since, as stated before, the range is much larger than the 5 NM ring, and as a result the probability for observed lightning and rain showers over the range is much higher than the 5 NM ring.

Specifically for percent correct in Figure 27, the measures for both lightning and rain showers appear to hide any significant differences between the HRRR and WINNDEX, particularly during early and late forecast periods when observed frequencies were low. However, probability of detection in Figure 28 shows much more variability between the HRRR and WINNDEX as well as between the range and the ring.

Another notable attribute to these results is that the daily diurnal cycle is indirectly presented in the skill measures. As daytime heating added to the instability of the environment, convection became more likely. This consequently created more hours with observed lightning and rain showers in the middle of the forecast period. This observation is reinforced by the frequency of occurrences, both observed and forecast.

One last key attribute is that despite the HRRR model's generally higher accuracy over WINNDEX, the probability of detection results in Figure 28 indicate a decrease in forecast performance during later hours of the forecast period. Generally, this occurs when the frequency of lightning and rain showers decreases after 22 UTC.

This is typical and expected from a numerical model and reinforces the principle that in operational weather forecasting, newer forecast model runs should be utilized when available due to their often more accurate forecasts. However, since the HRRR is a hourly updating model, the reduced performance in later forecast hours can potentially be mitigated with the use of new model runs as they become available.

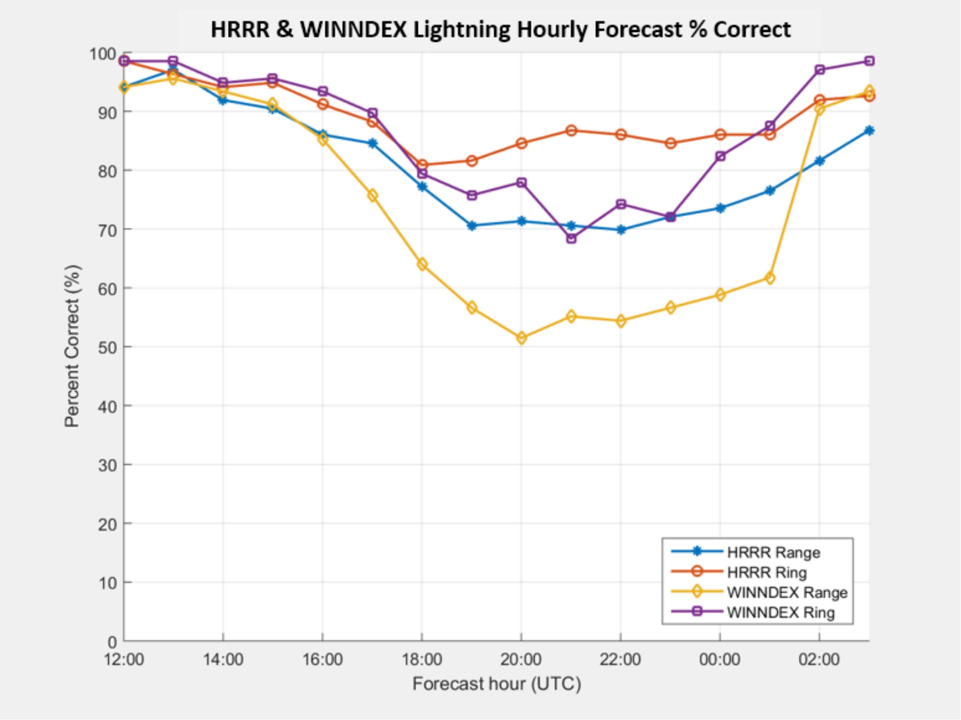

(a) Hourly lightning forecast percent correct results

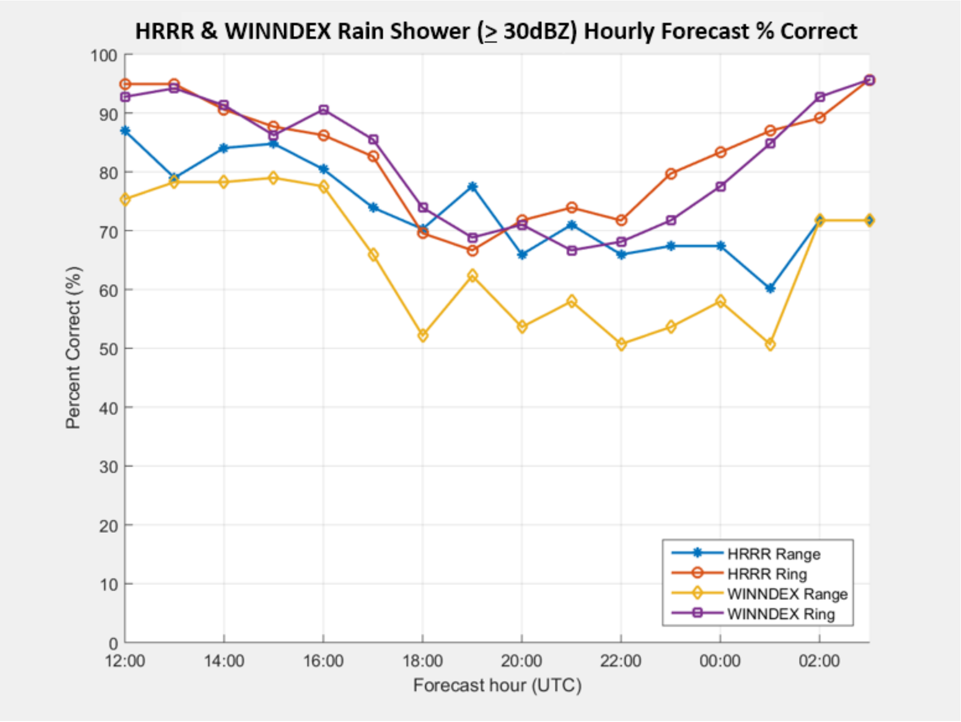

(b) Hourly rain shower forecast percent correct results

Figure 27. Hourly lightning and rain shower forecast percent correct results for HRRR model and WINNDEX over both the Eglin range complex and the 5 NM ring.

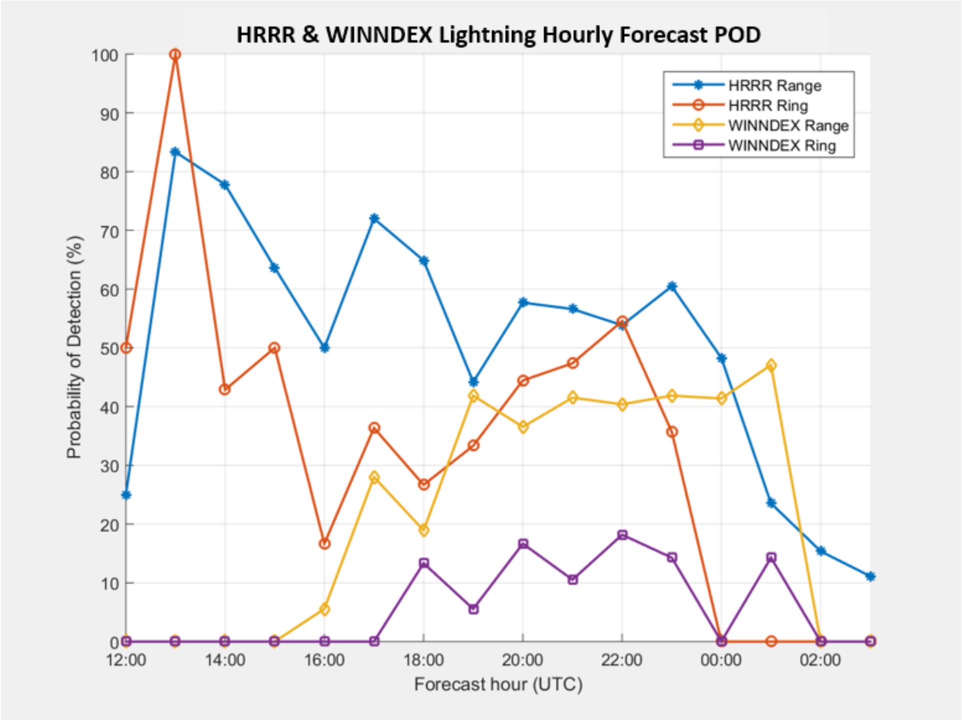

(a) Hourly lightning forecast probability of detection results

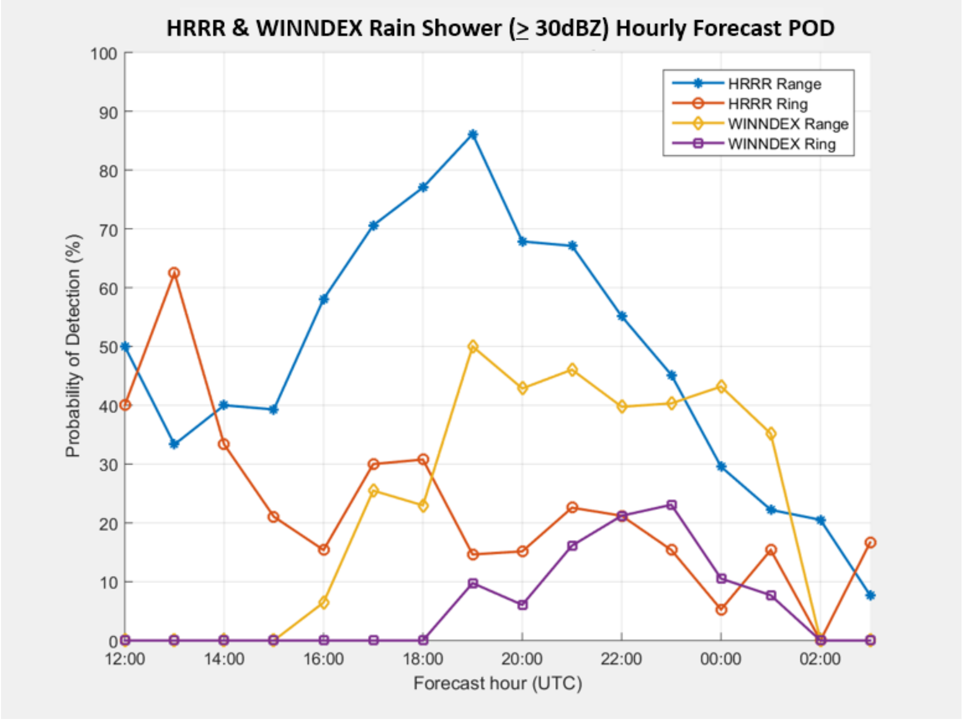

(b) Hourly rain shower forecast probability of detection results

Figure 28. Hourly lightning and rain shower forecast Probability of Detection results for HRRR model and WINNDEX over both the Eglin range complex and the 5 NM ring.

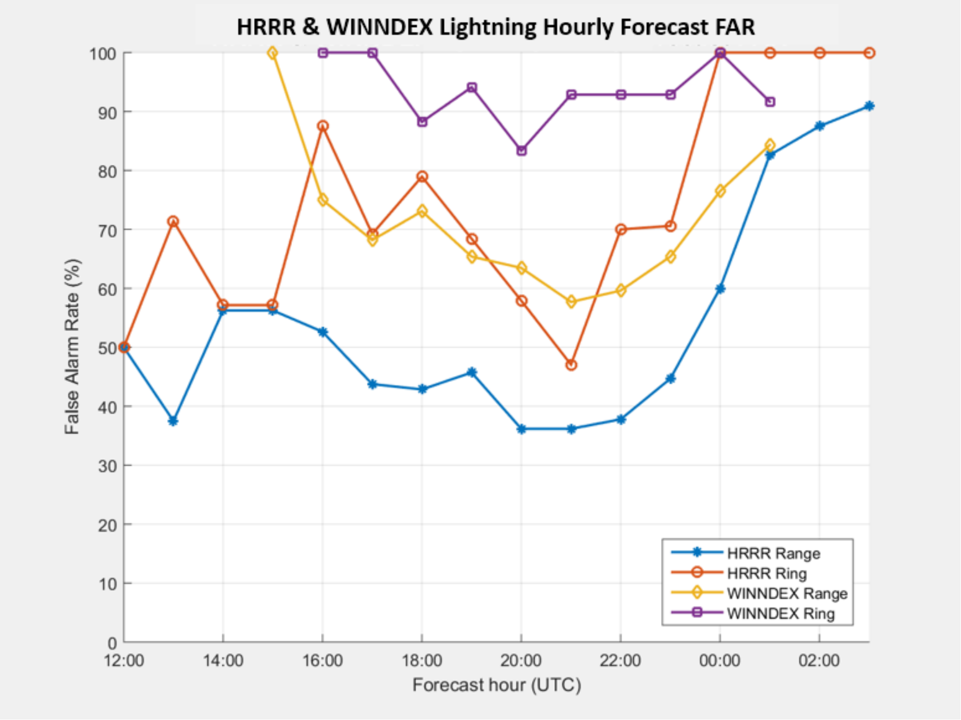

(a) Hourly lightning forecast false alarm rate results

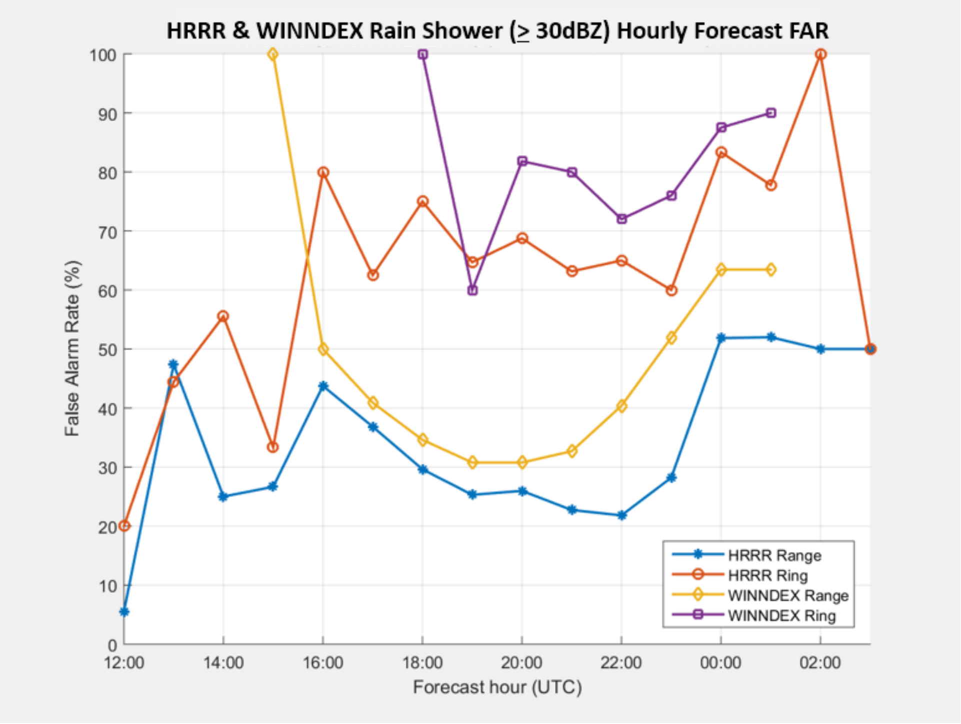

(b) Hourly rain shower forecast false alarm rate results

Figure 29. Hourly lightning and rain shower forecast false alarm rate results for HRRR model and WINNDEX over both the Eglin range complex and the 5 NM ring.

4.3 Daily Verification Results

Tables 5 and 6 contain the unfiltered daily verification results for the HRRR and WINNDEX.

Table 5. Unfiltered HRRR Daily Skill Measure Results.

	Eglin Range Complex		Eglin 5nm ring		Best Possible Value	Worst Possible Value
	Lightning	Rain Shower	Lightning	Rain Shower		
% Correct	77.9	84.6	75.7	52.2	100	0
POD	87.7	98.2	68.0	22.1	100	0
FAR	22	14.7	33.3	44.4	0	100
Bias	1.12	1.15	1.02	.40	1	> 1 or < 1
CSI	.70	.84	.51	.19	1	0
HSS	.53	.26	.48	.04	1	< 0
PSS	.51	.19	.48	.04	1	< 0

Table 6. Unfiltered WINNDEX Daily Skill Measure Results.

	Eglin Range Complex		Eglin 5nm ring		Best Possible Value	Worst Possible Value
	Lightning	Rain Shower	Lightning	Rain Shower		
% Correct	53.7	41.9	61.0	69.1	100	0
POD	76.9	98.1	46.9	20.0	100	0
FAR	56.0	60.5	70.6	81.5	0	100
Bias	1.75	2.48	1.59	1.08	1	> 1 or < 1
CSI	.39	.39	.22	.11	1	0
HSS	.14	.04	.10	0	1	< 0
PSS	.16	.05	.12	0	1	< 0

As indicated in the hourly verification, the HRRR has higher accuracy compared to WINNDEX. The HRRR's radar forecast for the range was associated with the best measures for percent correct, probability of detection, and false alarm rate. On the other hand, for the Heidke Skill Score and the Peirce Skill Score, the HRRR's lightning forecast for the range presented the best scores. This indicates that the lightning threat product provides a better forecast than simulated composite reflectivity when compared to the probability of the sample used in this study. However, this may also indicate that the radar occurrences simply have a higher frequency compared to lightning occurrences over the range.

For WINNDEX, the highest percent correct scores were actually for the 5 NM ring rather than the range. Unfortunately, this is likely due to the rarity of WINNDEX forecasts for lightning or rain showers for the 5 NM ring as well as the lower probability of an observed occurrence over the ring due to its small size when compared to the range. Evidence of this explanation is provided by the Heidke Skill Score and the Peirce Skill Score. The WINNDEX forecasts for lightning for the 5 NM ring are slightly better than the probabilities from the study sample, but the WINNDEX radar forecasts are no better than the probabilities from the study sample.

Tables 7 and 8 contain the unfiltered daily verification results for the HRRR and WINNDEX. As a reminder, filtered analysis omitted days which had some type of synoptic forcing such as frontal boundaries. This allowed an analysis that consisted only of days on which sea breeze and diurnal heating were the only forecast considerations for convection.

For the HRRR, forecast skill for some metrics appears to increase slightly after days were filtered from verification, but some measures indicate the opposite. The lack of significant change between filtered and unfiltered analysis is likely due to the small size of the study, only one warm season, and the fact that the HRRR, as a numerical weather prediction model, is designed to predict the future state of the atmosphere regardless of synoptic conditions. WINNDEX also shows similar mixed results between filtered and unfiltered analysis. However, WINNDEX was expected to gain skill from a filtered analysis due to its specific design to forecast thunderstorms and rain showers for sea breeze interactions at Eglin AFB.

Table 7. Filtered HRRR Daily Skill Measure Results.

	Eglin Range Complex		Eglin 5nm ring		Best Possible Value	Worst Possible Value
	Lightning	Rain Shower	Lightning	Rain Shower		
% Correct	80.2	84.5	76.7	52.6	100	0
POD	91.3	97.9	72.1	18.2	100	0
FAR	21.3	14.7	32.6	50.0	0	100
Bias	1.16	1.15	1.07	.36	1	> 1 or < 1
CSI	.77	.84	.53	.15	1	0
HSS	.57	.29	.51	.02	1	< 0
PSS	.55	.22	.52	.02	1	< 0

Table 8. Filtered WINNDEX Daily Skill Measure Results.

	Eglin Range Complex		Eglin 5nm ring		Best Possible Value	Worst Possible Value
	Lightning	Rain Shower	Lightning	Rain Shower		
% Correct	52.6	41.4	61.2	70.7	100	0
POD	79.1	97.7	52.0	15.0	100	0
FAR	57.5	61.5	71.7	85.0	0	100
Bias	1.86	2.53	1.84	1.00	1	> 1 or < 1
CSI	.38	.38	.222	.08	1	0
HSS	.14	.04	.12	-.03	1	< 0
PSS	.16	..06	.16	-.03	1	< 0

4.4 Timing Error

Figures 30 and 31 provide lightning timing error results for the range complex and the 5 NM range ring while Figures 32 and 33 provide rain shower timing error. Each plot provides initial onset timing error as well as the upper-level and low-level wind directions used in the WINNDEX process. Additionally, each plot contains the average "raw" timing error denoted by the blue line as well as absolute value timing error and data point count annotated in each figure. Raw refers to the timing error that is calculated with the inclusion of negative timing.

Once again, as with hourly verification and daily verification, timing error results indicate that the HRRR's forecasts are more accurate than WINNDEX. The main indication of this is the larger amount of data points for the HRRR when compared to the corresponding WINNDEX plots. In order to calculate timing error, a "yes" forecast and a "yes" observation had to exist, or in other words, "hits" had to occur. Thus the larger number of data points in HRRR timing error figures indicates a larger number of correct forecasts. In addition since WINNDEX has a high bias measure as indicated in Tables 6 and 8, the fact that it has less data points for timing error shows that despite WINNDEX's over-forecasting, WINNDEX has less correct forecast days for both lightning and rain showers.

The second indication that HRRR is more accurate than WINNDEX is the average raw timing error and absolute value timing error. The HRRR forecasts resulted with less than 60 minutes of raw average timing error in all occasions with the exception of rain shower timing error for the 5 NM ring. WINNDEX only managed to achieve less than 60 minutes of raw average timing error for lightning timing error over the range. For the absolute value timing error, the HRRR achieved a lower value in both lightning and rain showers for both locations. Thus, despite the HRRR having significantly more data points than WINNDEX, the HRRR achieved a lower timing error spread.

Lastly, with regard to the WINNDEX upper-level and low-level wind directions, there generally does not appear to be any trends in timing error. No wind categories indicated a bias for having positive or negative timing error. However, this does not necessarily prove that there is no trend since this study only covered a single warm season. More data could possibly show trends that are not obvious in this data set.

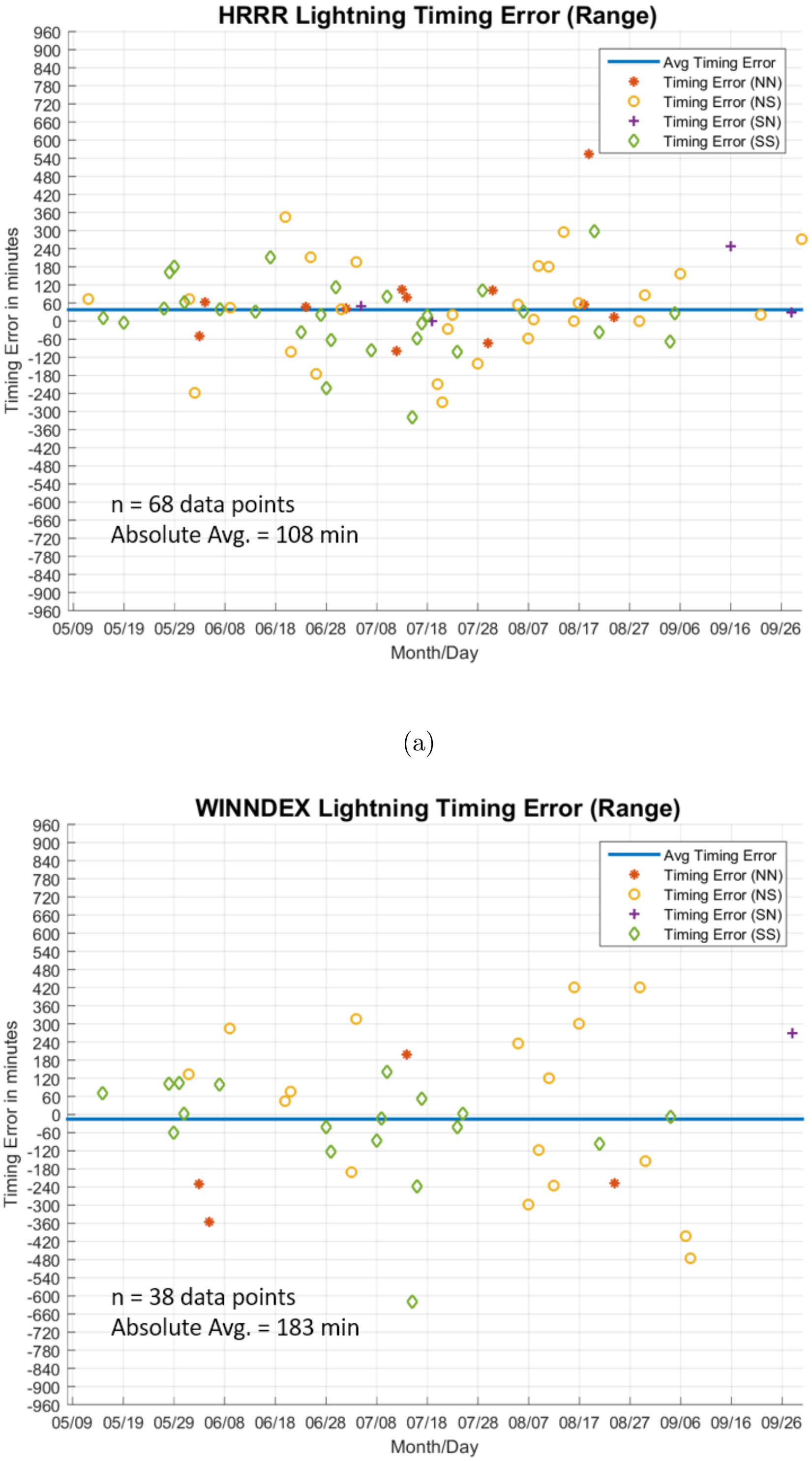

(a)

(b)

Figure 30. HRRR(a) and WINNDEX(b) lightning forecast timing error for the Eglin range complex. Timing error symbols represent WINNDEX wind direction where the first letter represents upper-level wind direction and the second letter represents low-level wind direction.

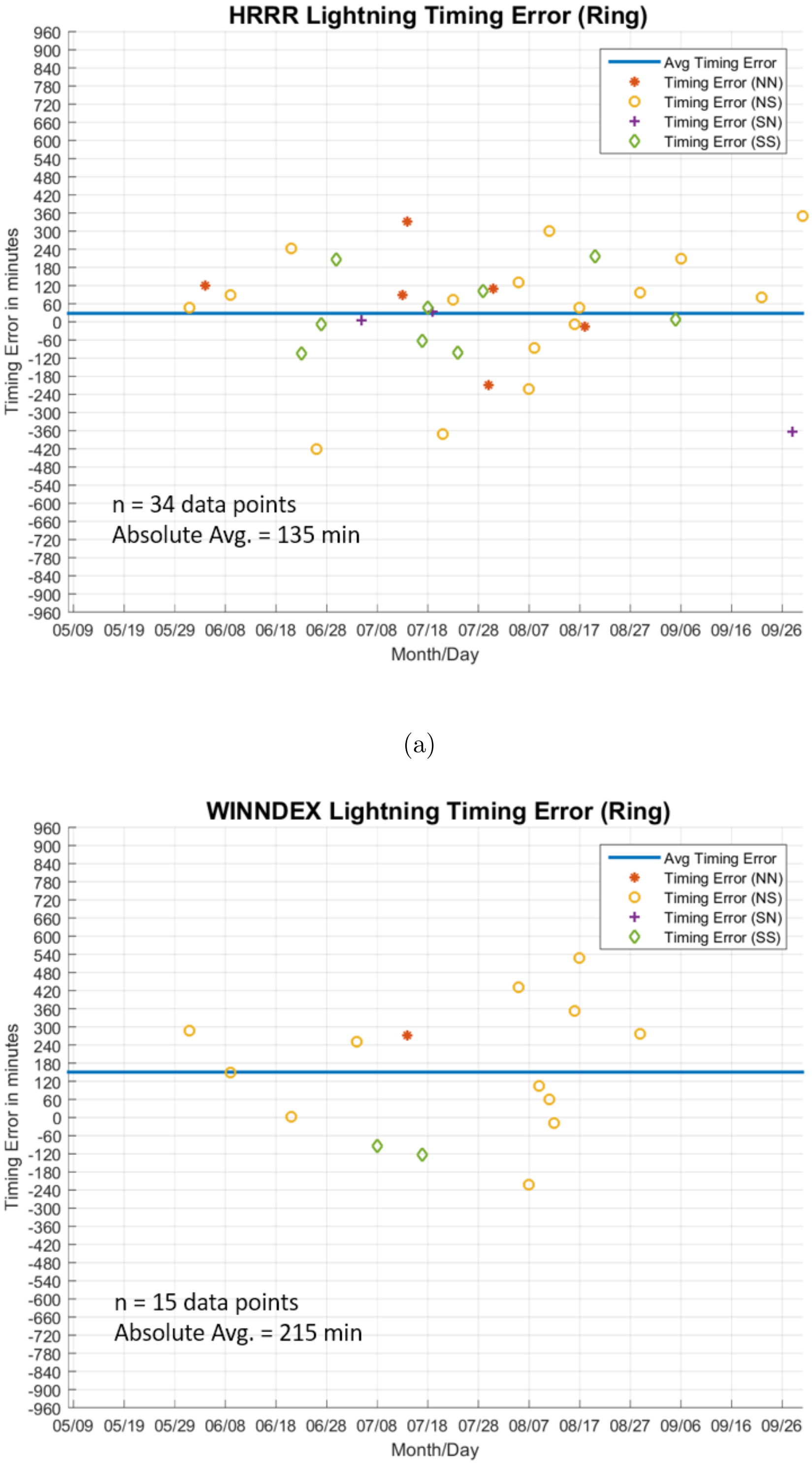

(a)

(b)

Figure 31. HRRR(a) and WINNDEX(b) lightning forecast timing error for the Eglin 5 NM range ring. Timing error symbols represent WINNDEX wind directions as annotated in Figure 30.

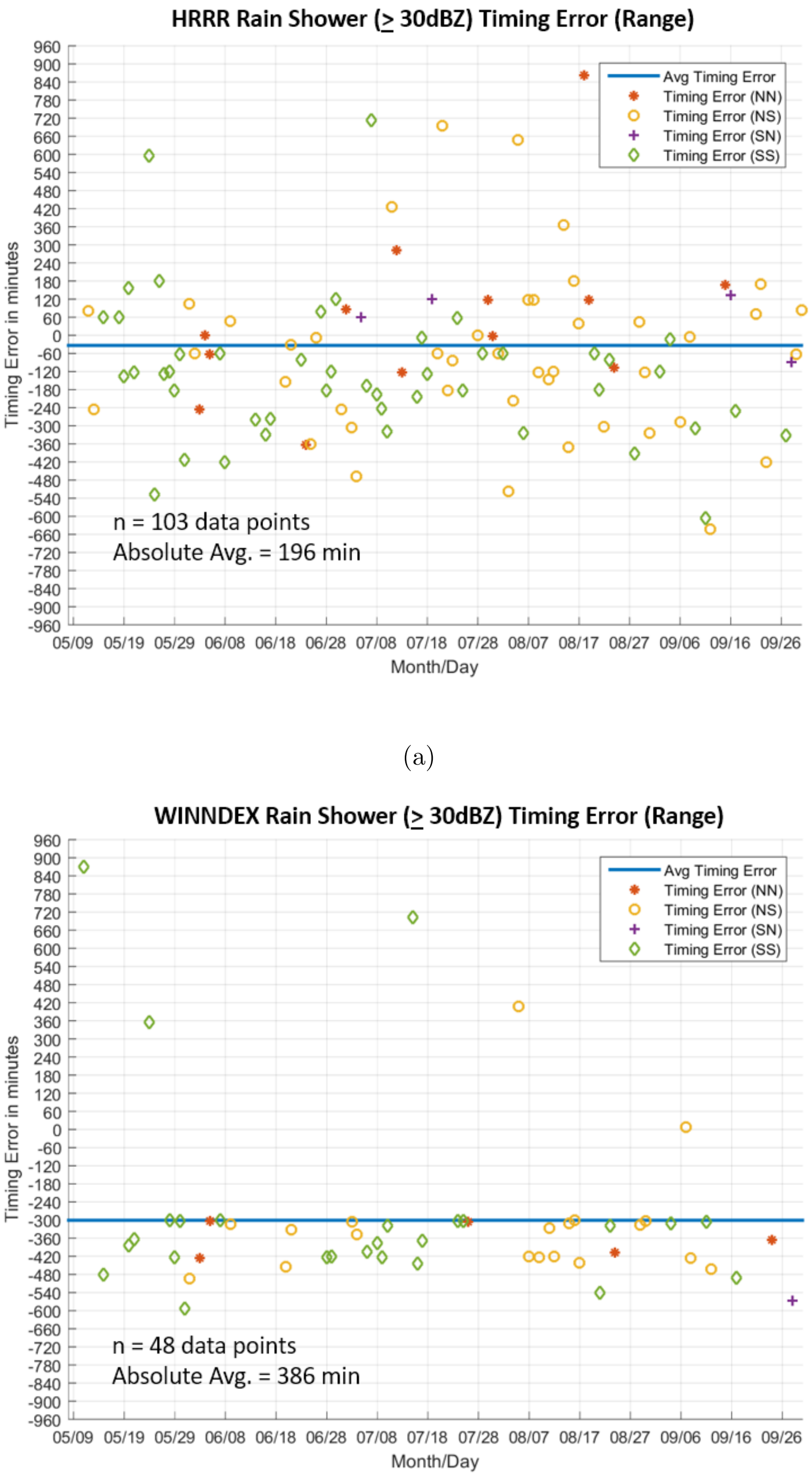

(a)

(b)

Figure 32. HRRR(a) and WINNDEX(b) rain shower forecast timing error for the Eglin range complex. Timing error symbols represent WINNDEX wind directions as annotated in Figure 30.

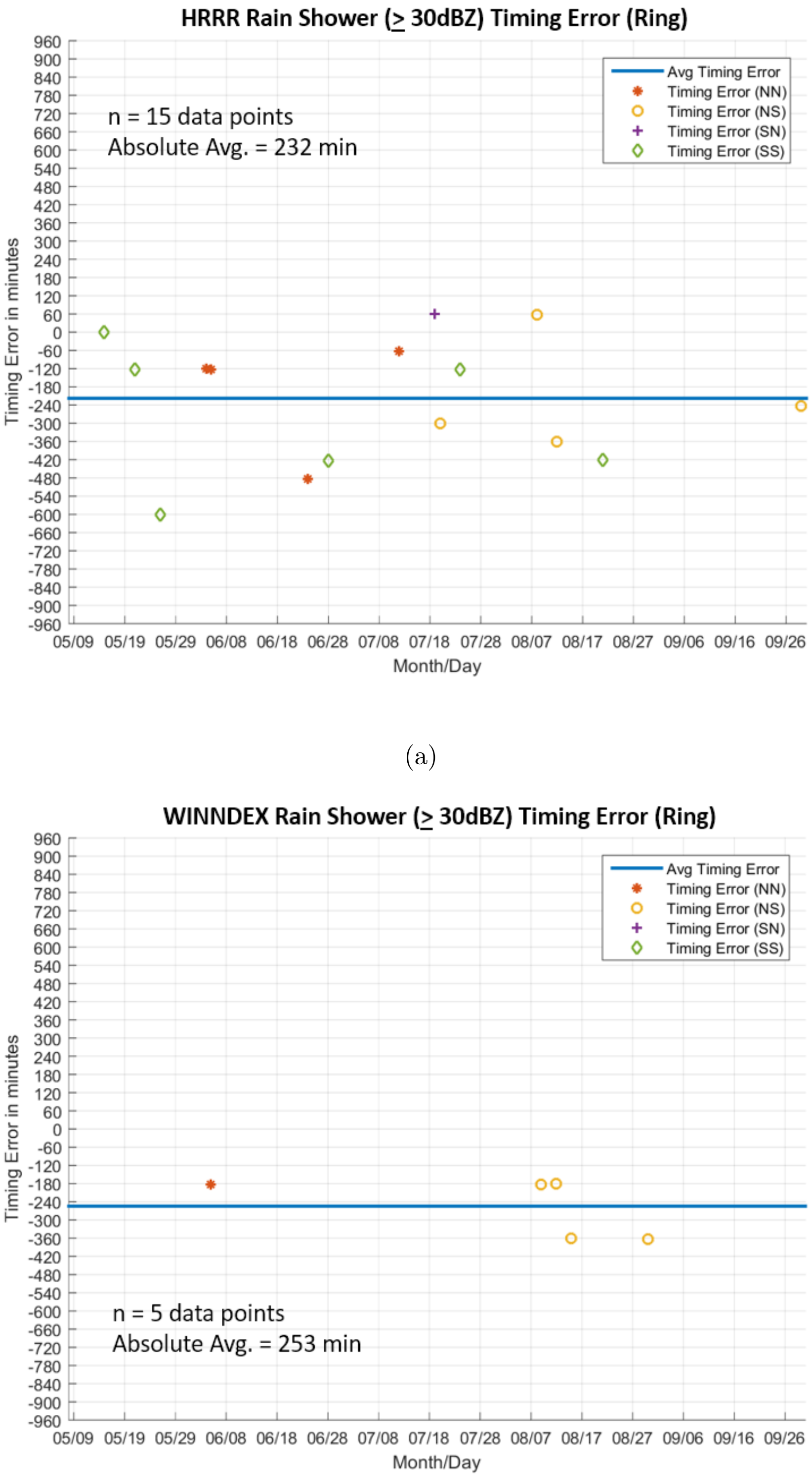

(a)

(b)

Figure 33. HRRR(a) and WINNDEX(b) rainshower forecast timing error for the Eglin 5 NM ring. Timing error symbols represent WINNDEX wind directions as annotated in Figure 30.

V. Conclusions

5.1 Summary

Based on this study, the HRRR model, in general, has higher forecast skill over the 96th Weather Flight's current WINNDEX method in forecasting lightning and rain showers. This determination is made based on the measures of skill for hourly verification and daily verification. In addition, initial onset timing error was evaluated and also indicated that overall HRRR has less timing bias and smaller absolute value timing error. Despite the HRRR model's performance, it is not without drawbacks. Based on hourly verification, forecast performance diminished significantly at later forecast hours, generally after 22 UTC. Also, based on daily verification results, because the 5 NM ring is much smaller than the Eglin range complex, HRRR forecast skill decreased significantly in all metrics for the 5 NM range ring, particularly for radar verification.

5.2 Recommendations for Future Work

One specific shortfall to this study was the small size of the data set. Because of the large size of HRRR files, model data is not available for long periods and files must be downloaded on a daily basis in order to ensure availability. This caused the study to span only one warm season. Thus, if further validation or study on sea breeze convection from the HRRR is desired, a more extensive data set may be useful.

With regard to WINNDEX, it too was made using only one warm season in its initial development. Considering this limitation as well as the WINNDEX now being nearly 30 years old, it would be beneficial to take several years of recent warm season data at Eglin AFB and possibly rewrite or recalibrate the nomograms. Also, with the literature suggesting the importance of initial wind direction and its effect on sea breeze front intensity, wind directions other than northerly or southerly may provide increased skill for WINNDEX. Additionally, because the 96th Weather Flight does not currently provide daily observed upper-air soundings, it may be beneficial to make common practice, if fiscally possible, the daily launch of warm-season radiosondes. This would create more accurate upper-air data for future research and eliminate the possible errors in using numerical weather prediction data to derive upper air information.

Lastly, because of insufficient time and data GRIB data availability, a numerical weather prediction approach involving ensembles could not be fully realized in this study. Air Force Weather's ensembles, which include resolution as fine as 4 km, should be evaluated and applied to the challenge of forecasting sea breeze thunderstorms. This would enable the determination of abilities and limitations of models specifically provided for Air Force operations. In addition, ensembles may assist in providing forecasters with bounds on possible forecast outcomes which deterministic models, such as the HRRR, simply can not provide.

Bibliography

14th Weather Squadron, 2015: Eglin AFB Operational Climatic Data Summary. Accessed 20 October 2015. [Available online at https://proxy.afccc.af.mil/OCDS-II/load.htm?locationID=ICAO_KVPS&reportType=html].

Arritt, R. W., 1993: Effects of the large-scale flow on charateristic features of the sea breeze. *J. Appl. Meteor.*, **32**, 116 – 124.

Atkins, N. T., and R. M. Wakimoto, 1997: Influence of the synoptic-scale flow on sea breezes observed during CaPE. *Mon. Wea. Rev.*, **125**, 2112 – 2130.

Azorin-Molina, C., S. Tijm, E. E. Ebert, S. M. Vicente-Serrano, and M. J. Estrela, 2014: Sea breeze thunderstorms in the eastern Iberian Peninsula. neighborhood verification of HIRLAM and HARMONIE precipitation forecasts. *Atmos. Res*, **139**, 101 – 115.

Baker, R. D., B. H. Lynn, A. Boone, W.-K. Tao, and J. Simpson, 2001: The influence of soil moisture, coastline curvature, and land-breeze circulations on sea-breeze-initiated precipitation. *J. Hydrometeor.*, **2**, 193 – 211.

Bechtold, P., J.-P. Pinty, and F. Mascart, 1991: A numerical investigation of the influence of large-scale winds on sea-breeze- and inland-breeze-type circulations. *J. Appl. Meteor.*, **30**, 1268 – 1279.

Benjamin, S., and Coauthors, 2015: NOAA/NWS SOO Science and Training Resource Center's 2014 Operational High Resolution Rapid Refresh (HRRR) training. Accessed 25 August 2015. [Available online at http://strc.comet.ucar.edu/library/Training/HRRR/].

Biggar, D. G., 1992: A mesoscale study of sea breeze enhanced summer thunderstorms in the Florida Panhandle. M.S. thesis, Florida State University.

Byers, H. R., and R. R. Braham Jr., 1948: Thunderstorm structure and circulation. *J. Meteor.*, **5**, 71–86.

Byers, H. R., and H. R. Rodebush, 1948: Causes of thunderstorms of the Florida Peninsula. *J. Meteor*, **5**, 275 – 280.

Camp, J. P., A. L. Watson, and H. E. Fuelberg, 1998: The diurnal distribution of lightning over north Florida and its relation to the prevailing low-level flow. *Wea. Forecasting*, **13**, 729–739.

Cornell, D., 1993: Thunderstorm forecast study for Eglin AFB, FL. Tech. rep., [Available online at http://www.dtic.mil/dtic/tr/fulltext/u2/a263423.pdf], United States Air Force.

EMC, 2015: National Stage IV QPE Product. Accessed 17 October 2015. [Available online at http://www.emc.ncep.noaa.gov//mmb/ylin/pcpanl/stage4/.].

Estoque, M. A., 1962: The sea breeze as a function of the prevailing synoptic situation. *J. Atmos. Sci.*, **19**, 244–250.

Gilliam, R. C., S. Raman, and D. D. S. Niyogi, 2004: Observational and numerical study on the influence of large-scale flow direction and coastline shape on sea-breeze evolution. *Bound-lay. Meteor.*, **111**, 275 – 300.

Holton, J. R., and G. J. Hakim, 2013: *An Introduction to Dynamic Meteorology*. 5th ed., Academic Press, Waltham, MA, 532 pp.

Homan, P., 2015: 96th Weather Flight mission brief.

Laird, N. F., D. A. R. Kristovich, R. M. Rauber, H. T. Ochs III, and L. J. Miller, 1995: The Cape Canaveral sea and river breezes: Kinematic structure and convective initiation. *Mon. Wea. Rev.*, **123**, 2942–2956.

Miller, S. T. K., B. D. Keim, R. W. Talbot, and H. Mao, 2003: Sea breeze: Structure, forecasting and impacts. *Rev. Geophys.*, **41**.

NCEI, 2015: Global Forecast System (GFS). Accessed 13 September 2015. [Available online at http://www.ncdc.noaa.gov/data-access/model-data/model-datasets/global-forcast-system-gfs].

NCEP, 2015: NCEP Central Operations: Model guidance (HRRR). Accessed 13 September 2015. [Available online at http://mag.ncep.noaa.gov/model-guidance-model-parameter.php?group=Model%20Guidance&model=HRRR&area=EAST-US&ps=area].

Pielke, R. A., 1973: A three-dimensional numerical model of the sea breezes over south Florida. *Mon. Wea. Rev.*, **1 (1)**, 201–208.

Roeder, W. P., 2013: Point paper on Earth Networks Total Lightning Network. Unpublished U.S. Air Force point paper available upon request from 14th Weather Squadron.

Rogers, R. R., and M. K. Yau, 1996: *A Short Course in Cloud Physics*. 3rd ed., Butterworth-Heinemann, Linacre House, Jordan Hill, Oxford OX2 8DP.

Snyder, J. P., 1982: *Map Projections - A Working Manual*. U.S. Geological Survey, [Available at https://pubs.er.usgs.gov/publication/pp1395].

UCAR, 2012: The COMET program: Weather Radar Fundamentals Accessed 6 March 2016. [Available online at http://www.meted.ucar.edu/radar/basic_wxradar/index.htm].

Vaisala, 2015: National Lightning Detection Network. Accessed 10 September 2015. [Available online at http://www.vaisala.com/en/products/thunderstormandlightningdetectionsystems/Pages/NLDN.aspx].

Wallace, J. M., and P. V. Hobbs, 2006: *Atmospheric Science: An Introductory Survey.* 2nd ed., Academic Press, San Diego, CA.

Weaver, J. C., 2006: The impact of synoptic-scale flow on sea breeze front propagation and intensity at Eglin Air Force Base. M.S. thesis, Naval Postgraduate School.

Welsh, P. T., P. Santos, and C. G. Herbster, 1999: A study of sea breeze convective interactions using mesoscale numerical modeling. *Natl. Wea. Dig.*, **23**, 33–45.

Wilks, D. S., 2011: *Statistical Methods in the Atmospheric Sciences.* 3rd ed., Academic Press, San Diego, CA.

Winn, R., 1995: WINNDEX: Eglin AFB local weather forecasting technique. Provided by 96th Weather Flight.

Zhong, S., and E. S. Takle, 1993: The effects of large-scale winds on the sealand-breeze circulations in an area of complex coastal heating. *J. Appl. Meteor.*, **32**, 1181–1195.

REPORT DOCUMENTATION PAGE	*Form Approved* *OMB No. 0704–0188*

1. REPORT DATE *(DD–MM–YYYY)* 03–24–2016	**2. REPORT TYPE** Master's Thesis	**3. DATES COVERED** *(From — To)* May 2014 — Mar 2016

4. TITLE AND SUBTITLE

Forecasting Sea Breeze Enhanced Thunderstorms at Eglin Air Force Base:
A Comparison Between Empirical Methods and the High Resolution Rapid Refresh Model

5a. CONTRACT NUMBER

5b. GRANT NUMBER

5c. PROGRAM ELEMENT NUMBER

6. AUTHOR(S)

King, Matthew P., Captain, USAF

5d. PROJECT NUMBER

5e. TASK NUMBER

5f. WORK UNIT NUMBER

7. PERFORMING ORGANIZATION NAME(S) AND ADDRESS(ES)

Air Force Institute of Technology
Graduate School of Engineering and Management (AFIT/EN)
2950 Hobson Way
WPAFB OH 45433-7765

8. PERFORMING ORGANIZATION REPORT NUMBER

AFIT-ENP-MS-16-M-074

9. SPONSORING / MONITORING AGENCY NAME(S) AND ADDRESS(ES)

557th Weather Wing
Attn: Dr. John Zapotocny
101 Nelson Drive
Offutt AFB, NE 68113
DSN 271-5520, COMM 402-294-5520

10. SPONSOR/MONITOR'S ACRONYM(S)

557 WW

11. SPONSOR/MONITOR'S REPORT NUMBER(S)

12. DISTRIBUTION / AVAILABILITY STATEMENT

DISTRIBUTION STATEMENT A:
APPROVED FOR PUBLIC RELEASE; DISTRIBUTION UNLIMITED.

13. SUPPLEMENTARY NOTES

This material is declared a work of the U.S. Government and is not subject to copyright protection in the United States.

14. ABSTRACT

Summer thunderstorms pose the greatest forecast challenge for the United States Air Force's 96th Weather Flight (96 WF) which provides weather support for Eglin Air Force Base (AFB). Located on Florida's panhandle, Eglin AFB encompasses the Department of Defense's largest range complex which covers 134,000 mi^2 $(347,000\ km^2)$ of water and 724 mi^2 $(1875\ km^2)$ of land. Due to the base's coastal location and unique coastline geometry, sea breeze is a dominant forecast consideration for thunderstorms. The 96 WF currently utilizes an empirical method, called WINNDEX, developed by former staff meteorologist Roger Winn to aid in thunderstorm forecasts. It combines the use of 12 UTC sounding data and nomograms to provide a forecast for Eglin's main base area and its land range. This study sought to compare the forecasts of the High Resolution Rapid Refresh (HRRR) model and WINNDEX. Final results indicated HRRR forecast skill surpassed WINNDEX in most metrics which included percent correct, probability of detection, false alarm rate, bias, critical skill index, Heidke Skill Score, Peirce Skill Score, and timing error.

15. SUBJECT TERMS

Eglin Air Force Base, sea breeze, thunderstorms, WINNDEX, High Resolution Rapid Refresh model

16. SECURITY CLASSIFICATION OF:			**17. LIMITATION OF ABSTRACT**	**18. NUMBER OF PAGES**	**19a. NAME OF RESPONSIBLE PERSON**
a. REPORT	**b. ABSTRACT**	**c. THIS PAGE**			Lt Col Kevin S. Bartlett, AFIT/ENP
U	U	U	UU	95	**19b. TELEPHONE NUMBER** *(include area code)* (937) 255-3636, x4520; Kevin.Bartlett@afit.edu

Standard Form 298 (Rev. 8–98)
Prescribed by ANSI Std. Z39.18